IMPLEMENTATION AND ASSESSMENT OF STATE ESTIMATION ALGORITHMS

IN SIMULATION AND REAL-WORLD APPLICATIONS

A Thesis
IN
Mechanical Engineering

Presented to the Faculty of the University
of Missouri–Kansas City in partial fulfillment of
the requirements for the degree

MASTER OF SCIENCE

by
PAUL JAMES KLAPPA

B. S., Rockhurst University, 2019

Kansas City, Missouri
2021

© 2021
PAUL JAMES KLAPPA
ALL RIGHTS RESERVED

IMPLEMENTATION AND ASSESSMENT OF STATE ESTIMATION ALGORITHMS IN SIMULATION AND REAL-WORLD APPLICATIONS

Paul James Klappa, Candidate for the Master of Science Degree

University of Missouri–Kansas City, 2021

ABSTRACT

State estimation algorithms are important mathematical tools for engineers and are capable of improving system modeling capabilities and scenario outcomes. Typically, systems utilize a variety of sensors to measure certain system states such as velocity or position; however, these sensors suffer from noise and biases which contaminate the states. Through implementing a state estimation algorithm, noise from low-cost sensors may be mitigated to provide better system state estimates. Thus, a need exists to apply these algorithms while using low-cost sensors and to assess the performance in different scenarios. The algorithms that were selected for analysis in this research were the Kalman Filter and Extended Kalman Filter, which were implemented in two separate experiments.

The first experiment encompassed a pursuer-evader scenario where the initial starting position of a pursuer and tracking measurement uncertainty of an evader were

varied. Position of the evader was determined through two methods: raw tracking sensor measurements and estimates from a Kalman Filter. In both cases, the tracking sensor uncertainty was parameterized as a single term to represent combined uncertainty from all possible noise sources. This experiment showed that an increase in sensor measurement uncertainty led to an increase in the mean miss distance for the pursuer for both the raw tracking sensor method and Kalman Filter method. However, most engagement resulted in the Kalman Filter method providing an improved position estimate of the evader, reducing the average miss distance by upwards of $50\,\%$.

In the second experiment, an Extended Kalman Filter was applied to an aircraft that experienced a multitude of free-flight hardware failures such as control surface and aerial delivery failures. The Extended Kalman Filter was designed to estimate the aircraft's stability and control derivatives along with the aircraft's dynamic states. Fixed-position aileron failures, ranging from -30° to 30°, were assessed and showed a loss of effectiveness in the control derivative state estimates. An aerial delivery failure from a bay located near the center of gravity resulted in small changes in some of the control derivatives and noise characteristics of the aircraft; however, a payload release failure from a bay located on the wing resulted in every state estimate changing. Post-failure state estimate changes indicate the potential of implementing fault isolation control schemes to mitigate the failure after initial detection.

This research explored the usage of applying two state estimation algorithms to

expand the modeling capabilities of two systems. Not only did the algorithms provide improved estimates for system states, the states that did not have direct sensor measurements were accurately estimated. Furthermore, the algorithms were tailored to each scenario and successfully utilized low-cost sensors to improve the scenario results.

APPROVAL PAGE

The faculty listed below, appointed by the Dean of the School of Computing and Engineering, have examined a thesis titled "Implementation and Assessment of State Estimation Algorithms in Simulation and Real-World Applications," presented by Paul James Klappa, candidate for the Master of Science degree, and hereby certify that in their opinion it is worthy of acceptance.

Supervisory Committee

Travis Fields, Ph.D., Committee Chair
Department of Civil & Mechanical Engineering

Mujahid Abdulrahim, Ph.D.
Department of Civil & Mechanical Engineering

Roy Allen, Ph.D.
Department of Civil & Mechanical Engineering

Anthony Caruso, Ph.D.
Department of Physics & Astronomy

CONTENTS

NOMENCLATURE

STATE ESTIMATION IN A TRACKING-BASED PURSUER-EVADER SCENARIO

SR	=	Speed ratio of the pursuer to the evader
$U_{tracking}$	=	Tracking uncertainty ($95\,\%$ Confidence Interval), m
v_e	=	Velocity of the evading aircraft, m/s
v_p	=	Velocity of the pursuing aircraft, m/s
ω_p	=	Pursuer turn rate, deg/s
ρ	=	Radius of curvature, m
a_n	=	Normal acceleration, m/s^2
LOS	=	Line of sight angle, deg
$\dot{LOS}$	=	Line of sight rate, deg/s
N	=	Proportional navigation gain
H_k	=	Measurement to state connection matrix
P_k	=	Kalman Filter error state covariance matrix
Q_k	=	Kalman Filter process noise covariance matrix
R_k	=	Kalman Filter measurement noise covariance matrix
x_k	=	Kalman Filter state vector
z_k	=	Kalman Filter sensor measurement vector
ϕ_k	=	Kalman Filter state transition matrix

ASSESSMENT OF FIXED-WING UAV SYSTEM IDENTIFICATION MODELS DURING ACTUATOR AND PAYLOAD DROP FAILURES

α	=	Angle of attack, deg
β	=	Sideslip angle, deg
$\{p, q, r\}$	=	Reference roll, pitch, and yaw axis rates, deg/s
$\{\dot{\beta}, \dot{p}, \dot{r}, \dot{\phi}\}$	=	Lateral aircraft state derivatives
$\{\dot{\alpha}, \dot{q}\}$	=	Longitudinal aircraft state derivatives (Short-Period Approximation)
$\{L, M, N\}$	=	Aerodynamic moment components in body reference frame

$\{X, Y, Z\}$	=	Aerodynamic force components in body reference frame
$\{I_x, I_y, I_z\}$	=	Moment of inertia components about the body reference frame
$\{A_\phi, A_\theta, A_\psi\}$	=	Amplitude of roll, pitch, and yaw multi-sine input
b	=	Wingspan, m
$\bar{c}$	=	Mean wing chord, m
g	=	Gravitational constant, m/s^2
m	=	Aircraft mass, kg
$\bar{q}$	=	Dynamic pressure, kg/ms^2
ρ	=	Density of air, kg/m^3
S	=	Planform surface area, m^2
θ_0	=	Trimmed pitch angle, deg
v_0	=	Reference flight velocity, m/s
x_a	=	X-axis angle of attack sensor position, m
y_a	=	Y-axis angle of attack sensor position, m
C_{Y_β}	=	Dimensionless Y-axis force derivative coefficient with respect to sideslip
C_{Y_p}	=	Dimensionless Y-axis force derivative coefficient with respect to roll rate
C_{Y_r}	=	Dimensionless Y-axis force derivative coefficient with respect to yaw rate
$C_{Y_{\delta a}}$	=	Dimensionless Y-axis force derivative coefficient with respect to rudder deflection
C_{l_β}	=	Dimensionless Roll moment derivative coefficient with respect to sideslip
C_{l_p}	=	Dimensionless Roll moment derivative coefficient with respect to roll rate
C_{l_r}	=	Dimensionless Roll moment derivative coefficient with respect to yaw rate
$C_{l_{\delta a}}$	=	Dimensionless Roll moment derivative coefficient with respect to aileron deflection
$C_{l_{\delta r}}$	=	Dimensionless Roll moment derivative coefficient with respect to rudder deflection
C_{n_β}	=	Dimensionless Yaw moment derivative coefficient with respect to sideslip
C_{n_p}	=	Dimensionless Yaw moment derivative coefficient with respect to roll rate
C_{n_r}	=	Dimensionless Yaw moment derivative coefficient with respect to yaw rate
$C_{n_{\delta a}}$	=	Dimensionless Yaw moment derivative coefficient with respect to aileron deflection
$C_{n_{\delta r}}$	=	Dimensionless Yaw moment derivative coefficient with respect to rudder deflection
C_{L_α}	=	Dimensionless Lift force derivative coefficient with respect to angle of attack

C_{L_q}	=	Dimensionless Lift force derivative coefficient with respect to pitch rate
$C_{L_{\delta e}}$	=	Dimensionless Lift force derivative coefficient with respect to elevator deflection
C_{m_α}	=	Dimensionless Pitch moment derivative coefficient with respect to angle of attack
C_{m_q}	=	Dimensionless Pitch moment derivative coefficient with respect to pitch rate
$C_{m_{\delta e}}$	=	Dimensionless Pitch moment derivative coefficient with respect to elevator deflection
F_k	=	Extended Kalman Filter state transition matrix
G	=	Extended Kalman Filter measurement matrix
I	=	Identity matrix of size $n \times n$
n	=	Number of estimated states in the Extended Kalman Filter
P	=	Extended Kalman Filter error covariance matrix
Q	=	Extended Kalman Filter process noise covariance matrix
R	=	Extended Kalman Filter measurement noise covariance matrix
x_k	=	Extended Kalman Filter state vector
z_k	=	Extended Kalman Filter sensor measurement vector

ILLUSTRATIONS

TABLES

ACKNOWLEDGEMENTS

Funding for this research was provided by the Office of Naval Research under N00014-17-1-3016. Thank you to the members of the Parachute and Aerial Vehicle Systems Lab at UMKC who helped conduct flight tests and provided me with valuable feedback including Shawn Herrington, Cody Smith, and Simeon Karnes; this research would not have been possible without your support.

CHAPTER 1

INTRODUCTION

1.1 System Identification

Developing accurate mathematical models for physical systems has always been a fundamental goal for engineers; however, these mathematical models are subject to imperfect sensor measurements and biases. Sensor measurement error contaminates the models resulting in erroneous output for different input parameters [1]. Thus, the development of improved system models, also referred to as system identification, has been an important consideration throughout the last century to the present. The purpose of this research is to explore system identification through the application of state estimation algorithms and to assess the impact of uncertainty from low-cost sensors. Such algorithms are considered state estimators/filters and include the Kalman Filter and Extended Kalman Filter, both of which will be discussed in this research.

1.2 State Estimation Algorithms

The well-known Kalman Filter (KF), pre-dating NASA's Apollo missions, revolutionized the aerospace industry and is considered the standard for state estimation algorithms. This filter was designed as a means of linearizing a system such that a system's states, e.g. position or velocity, are estimated without requiring direct sensor measurements for each system state. The Kalman Filter defined the state-of-the-art for modeling

and built the foundation for its successor, the Extended Kalman Filter. Furthermore, the entrance of the Kalman Filter paved the way for consideration of other complex state estimation algorithms like the Unscented Kalman Filter [2], Federated Kalman Filter [3], and Interacting Multiple Models [4].

Typically, physical systems that require high precision measurements, such as a spacecraft and aircraft, utilize expensive sensors and instrumentation which are impractical and prohibitive for most other applications (i.e. a quadrotor which requires angular velocity measurements from at least three axes). For applications where highly accurate sensors are unavailable due to cost restrictions, a system may suffer more from sensor noise which reduces the accuracy of the system's models. However, the added sensor noise can be accounted for through implementation of state estimation algorithms, which aim at separating the signal from the noise. The paradigm requiring highly accurate sensors for highly accurate models has shifted, and state estimation algorithms now fill the void created from using low-cost sensors.

State estimation algorithms have expanded system modeling capabilities by modeling more state variables; however, it may be unclear exactly when implementation of these algorithms is justified. Thus, two different experiments were considered in this study to provide instances when certain state estimation algorithms might apply. Without implementing these state estimation algorithms, the modeling potential of the systems is limited, resulting in the inability of estimating important system states. The limited modeling potential is explored in the first experiment as comparative conclusions are drawn between utilizing and not utilizing a Kalman Filter. The second experiment explores the

expansion of the modeling potential for an aircraft that experiences free-flight hardware failures.

The first experiment, which uses a Kalman Filter, assesses four tracking sensor uncertainties and their impact on a pursuer-evader engagement. The Kalman Filter utilized simulated tracking measurements based on four different uncertainty values. The main objective of this scenario is to explore whether or not the miss distance for the pursuer improved with the Kalman Filter as opposed to only using the raw tracking sensor measurements. This scenario also explored the benefits of the Kalman Filter and the resultant state estimates associated with the evader.

The second experiment used an Extended Kalman Filter to estimate an aircraft's linearized longitudinal and lateral-directional dynamic states while using inexpensive sensors to detect and explore effects from catastrophic aircraft failures. The objectives for this experiment were to determine changes in the dynamic models and to estimate the aircraft's stability and control derivatives along with the aircraft states before and after free-flight failures occurred. The free-flight failures that the aircraft experienced were control surface failures and two different aerial delivery failures. The failures outlined the ability of the Extended Kalman Filter to detect changes in the aircraft's dynamics while simultaneously exploring payload-based use cases.

1.3 Summary of Contributions

The main contributions of this work are as follows:

- **A Kalman Filter was implemented and assessed in a pursuer-evader scenario**

by varying tracking sensor uncertainty in a simulation environment.

  - **Reduction of pursuer miss distance was demonstrated when using the KF estimation method as opposed to using raw tracking measurements.**
  - **Effects from different tracking sensor uncertainty levels were evaluated during different pursuer starting conditions.**

- **An Extended Kalman Filter was implemented and assessed for fault detection and expansion of modeling capabilities using inexpensive sensors.**

  - **Estimation of longitudinal and lateral-directional dynamic states was demonstrated before and after free-flight hardware failures occurred.**
  - **Effects from control surface failures and aerial delivery failures were evaluated.**

1.4 Thesis Organization

This thesis is organized as follows. First, a literature review is discussed which details Kalman Filter and Extended Kalman Filter historical information. Then other researchers' work associated with the pursuer-evader scenario and fault detection scenario are discussed. Next a detailed description of the first experiment, the pursuer-evader engagement, is discussed which includes specific simulation parameters and Kalman Filter parameters. Next, the results of running this simulation with and without a Kalman Filter are compared and conclusions are drawn regarding the state estimation method. The

fourth chapter details the second experiment, which focused on implementing an Extended Kalman Filter to evaluate different free-flight hardware failures. This chapter also discusses aircraft dynamics, parameters related to the Extended Kalman Filter, and results from the free-flight tests. Finally, big picture conclusions regarding the Kalman Filter and Extended Kalman Filter are drawn while also discussing future work.

CHAPTER 2

LITERATURE REVIEW

2.1 Kalman Filter

The Kalman Filter (referred to as KF hereafter) was introduced in the 1960s approximately 20 years after Wiener filter theory was developed. Wiener's method had focused on minimizing mean-square error in the time domain which was considered to be least-squares filtering [2]. However, the benefit of the filter developed by R.E. Kalman was the usage of state-space models with discrete sensor measurements [5]. The description and steps for the discrete Kalman Filter will be discussed in Chapter 3 and are expanded further in [2]. The importance of the KF was discovered during the 1960s when the algorithm resulted in major progress for NASA's Apollo missions. The development of this algorithm was headed by the Dr. R.E. Kalman along with R.S. Bucy at the Research Institute for Advanced Studies when the approach to linear filtering was published for discrete and continuous time models [5, 6]. The chief of the Dynamics Analysis Branch at NASA, S.F. Schmidt, invited Dr. Kalman to present on the topic of this algorithm at Ames Research Center. This event led to the development and application of the Extended Kalman Filter in the circumlunar navigation simulation on a 36-bit floating computer [7, 8].

The wide acceptance was illustrated through the KF's implementation during the mid-1960s when the algorithm was integrated into the C5A aircraft [9]. Similarly, the

KF has been used for inertial navigation, radar tracking, and the development of the Global Positioning System (GPS) [7, 10]. Research areas related to economic time series forecasting and smoothing [11–13] along with medical applications [14] have also implemented the KF. The list of applications is not exhaustive and only touches on some of the earliest work related to KFs.

Recently, however, the KF has been applied to applications related to bio-mechanics and motion capture. One research used multiple KF-based algorithms for lower body motion capture [15]. The algorithms eliminated the use of magnetometers to correct for yaw angle drift error while a test subject performed walking, jumping, jogging, and stair-stepping maneuvers. The proposed design for the system proved to be robust against magnetic disturbances and showed a high level of accuracy for its estimated states [15]. Another motion capture related application was the design of a body suit which used a KF [16]. This application used position sensor data and body position data coupled with a KF to yield a virtual representation of the wearer's body in real-time.

2.2 Extended Kalman Filter

The Extended Kalman Filter (EKF) was developed in the 1960s, as previously mentioned in Section 2.1, and was used in the circumlunar navigation simulation for NASA [7]. The development of this algorithm was monumental for the aerospace industry and became popular in other fields as well. The EKF was popular as it introduced quasi-linearized applications to the linearized solution space [9].

One application of the EKF was for longitudinal stability derivative and aircraft

state estimation [17]. A 3-2-1-1 multi-step input was used on an aircraft elevator to excite the longitudinal dynamics. The method used in this research resulted in parameter convergence within $10\,\mathrm{s}$ [17]. A similar usage of the EKF was researched by M. Curvo and also resulted in estimation of the longitudinal aerodynamic derivatives [18]. Other researchers utilized an EKF for short-period estimation [19] and lateral aerodynamic derivative estimation [20].

2.3 Pursuer-Evader Scenario

Pursuer-evader scenarios, similar to the one explored in this research, have been popular in game theory and military strategy since the 1950s. One of the earliest sources explores the fundamentals of game theory and defines these engagements as differential games [21]. This book details the theories behind a multitude of differential games which expand into applications of warfare and control optimization problems. One notable differential game is "The Game of Two Cars." This differential game imposes turn rate limitations and maximum speed constraints on both the pursuer and evader. A capture occurs if the pursuer's speed is higher than that of the evader [21]. This scenario was expanded on by other authors who considered curvature constraints and outlined proofs related to the pursuer's ability to capture the evader [22, 23].

Higher fidelity experimentation and simulation has been assessed and has typically focused on a missile-based pursuer which utilizes a KF to reduce the miss distance with its target [24, 25]. These engagements focus on the endgame portion of flight while using a variety of sensors and control logic. Other experiments focus on using slightly

different KF algorithms like mixture KFs, which rely on a stored bank of KFs [26]. Other research explores the engagement from a non-linearized point of view using an infrared homing missiles with an EKF [27]. Similarly, other research has looked at generalized pursuers which compare the EKF's performance between an onboard sensor and a ground radar [28, 29].

Particle Filters have also been implemented for pursuer-evader research, which focused on coordinated pursuit scenarios [30]. The authors described the issue of searching until detection occurs and then capturing thereafter using combined observation likelihoods and weighted expected states. The first scenario that was assessed by the authors was a coordinated effort with three pursuers and a single evader. The second scenario involved three evaders and four pursuers. In both scenarios, the particle filter proved to be robust and useful for engaging multiple targets [30].

2.4 Aircraft Fault Detection Scenario

Free-flight failures are a component of the second experiment in this thesis and are a popular topic for the aerospace industry. These free-flight failures may result in catastrophic results and must be evaluated to improve the robustness of an aircraft. Researched conducted by R. Venkataraman and P. J. Seiler looked at split rudder fixed-position failures, where the rudder control surface becomes stuck at a particular deflection angle [31]. This research highlights the need for failure detection along with failure isolation. Typically, these failures require reconfigurable controllers in order to account for the fixed-position failure. The authors used high fidelity simulations to assess analytical and

hardware-based redundancy. Hardware redundancy was achieved through splitting the rudder, and analytical redundancy was achieved through implementing a fault detection and isolation filter. The simulation showed that the stuck rudders (top and bottom) were detectable through different resulting aileron commands [31].

Other work associated with fault and anomaly detection was done by A. Keipour et. al. [32]. This research focused on using a real-time approach employing the recursive least squares method. Modeling was done through signal pairs instead of the entirety of the aircraft dynamics. This simplification makes this type of modeling applicable to more unmanned aircraft systems as the dynamics vary from aircraft to aircraft [32]. The authors tested control surfaces that became stuck at zero degree positions, engine power loss, and maximum stuck deflection angles with the rudder. This work resulted in only two false positives and two false negatives out of 22 tests [32].

Fault tolerance was also researched by J. D. Boskovic et. al., which details the implementation of adaptive interacting multiple observers [33]. This method realizes that each type of failure results in different changes within the aircraft dynamics. The change in dynamics is accounted for by using multiple models that represent the different failure conditions along with the nominal flight condition [33].

A method of fault tolerance based on sensor faults is explored by A. Carlson and M. Berarducci, which uses a Federated Kalman Filter (FKF) to partition sensors into localized filters and then combines the solutions into a master filter [3]. The FKF was applied to a navigation system comprised of inertial navigation sensors, GPS, and radar. The authors note that centralized Kalman Filters suffer from gradual sensor failures whereas

the FKF minimizes the impact of a gradual sensor failure due to the partitioned structure and performance mode. One advantage to using the FKF is the ability to receive sensor measurements asynchronously with minimal sensor observation losses. The authors note that a non-inertial navigation sensor fault during the experimentation did not contaminate each local filter (in the case of a FKF no reset mode); thus, the efficacy of the non-faulty local filters, which uniquely retain all of the system information, remains uncontaminated [3].

CHAPTER 3

STATE ESTIMATION IN A TRACKING-BASED PURSUER-EVADER SCENARIO

This chapter discusses a pursuer-evader simulation environment that was developed using MATLAB® to analyze the impact of tracking sensor uncertainty along with enabling and disabling the usage of a KF. First, the MATLAB® simulation environment will be discussed along with the KF setup. Next, the non-KF results will be assessed for different pursuer and evader initial conditions and tracking measurement uncertainty levels. The KF-based approach is then presented and compared to the non-KF approach during the same scenarios. Finally, the overall results are discussed and conclusions are drawn regarding the implementation of the KF.

3.1 Methodology

3.2 Pursuer-Evader Simulation

A simulation environment was developed in MATLAB® in order to compare the effects of using simulated tracking sensor measurements with and without a KF. Miss distance, defined as the closest distance between the pursuer and the evader, was used as a baseline comparison between non-KF and KF estimation. The miss distance also represents the minimum Euclidean distance between the pursuer and evader during the simulation. Furthermore, time of miss distance was also considered. The simulation was developed such that an evading aircraft starts from the origin and flies due North with

a fixed velocity. A second aircraft, the pursuer, attempts to intercept the evader. The pursuer and evader scenario uses parameters like tracking sensor uncertainty and initial positions that relate to endgame. Endgame is defined as the last portion of a pursuer-evader engagement, and was considered to last $20\,\mathrm{s}$ in this simulation. Thus, the pursuer's starting position and heading were controlled such that perfect tracking measurements of the evader would result in direct interception in $20\,\mathrm{s}$. However, $20\,\mathrm{s}$ interception is not always possible since tracking sensor uncertainty contaminates the evader's position estimates. Thus, the simulation was set to run for at most $40\,\mathrm{s}$ as this provides enough time for an interception when noise is added to the engagement. Throughout the simulation, the pursuer uses proportional navigation (PN) to fly toward the evader's position based on non-KF measurements and then based on KF position estimates. It is important to note that the evader has no knowledge of the pursuer's location during the engagement.

The objective of this experiment was to provide miss distance performance comparisons between non-KF position estimation and KF position estimation while using four different tracking sensor uncertainties. The tracking sensor uncertainty combines all noise sources into a single uncertainty parameter. Usage of a combined uncertainty parameter means that simulation results can apply to a variety of uncertainty parameters without testing individual combinations of specific uncertainty sources. The tracking uncertainty in this simulation can be described by a $95\,\%$ confidence interval ($\pm\ 2\sigma$), as shown in Table 1. This single uncertainty value is useful, for instance, if a miss distance of $5\,\mathrm{m}$ is required for the pursuer, then the scenario may only succeed if a KF is used with a tracking sensor that has a measurement standard deviation of $25\,\mathrm{m}$. Table 1 shows

four uncertainty values with their respective standard deviation and variance. The latter is included since these values are used in a KF.

Table 1: Tracking sensor uncertainty bounds based on the $95\,\%$ confidence interval.

Tracking Uncertainty ($95\,\%$ **CI**)	**Standard Deviation**	**Variance**
$100\,\mathrm{m}$	$50\,\mathrm{m}$	$2500\,\mathrm{m}$
$50\,\mathrm{m}$	$25\,\mathrm{m}$	$625\,\mathrm{m}$
$20\,\mathrm{m}$	$10\,\mathrm{m}$	$100\,\mathrm{m}$
$2\,\mathrm{m}$	$1\,\mathrm{m}$	$1\,\mathrm{m}$

3.2.1 Simulation Parameters & Setup

The simulation uses five different starting positions for the pursuer and one starting position for the evader. The starting positions for the pursuer are calculated from the $20\,\mathrm{s}$ endgame which uses a kinematic solution for direct intercept. The starting position for the pursuer and evader are shown in Figure 1. Each of the five selected starting positions for the pursuer have a relative heading angle from the evader, which points the pursuer's heading along the projected path of the evader. The relative heading angles that were chosen for this simulation were $0°$, $45°$, $90°$, $270°$, and $315°$. Other possible starting conditions are shown in Figure 2, which provides time of intercept and heading for the pursuer and evader at any starting position.

This simulation uses a speed ratio of 1.5:1, which means the pursuer is 1.5 times the speed of the evader. The simulation parameters are provided in Table 2. The pursuer is able to perform turns with a G-limit of 5 (5*$9.81\,\mathrm{m/s^2}$). In order to determine the turn rate, the normal acceleration equation is used, $a_n = \dfrac{v_p^2}{\rho}$ (a subscript p is indicative of

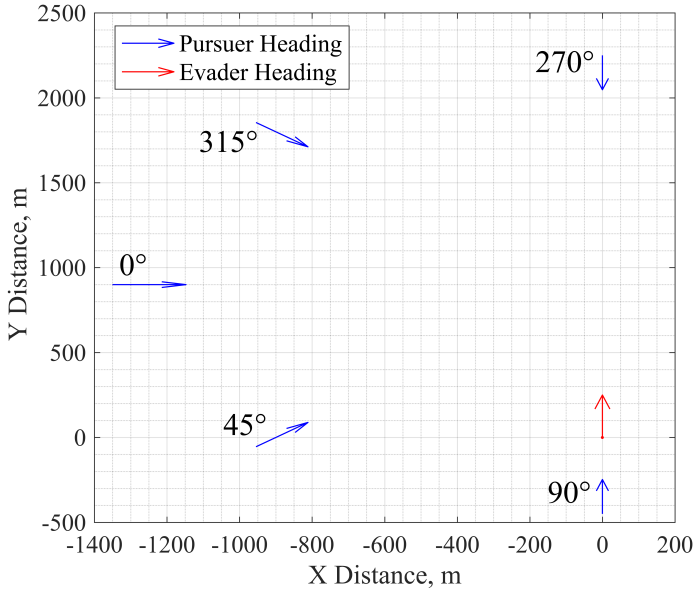

Figure 1: Pursuer and evader starting positions and headings for the simulation. These initial conditions lead to direct interception of the evader at 20 s using perfect tracking measurements.

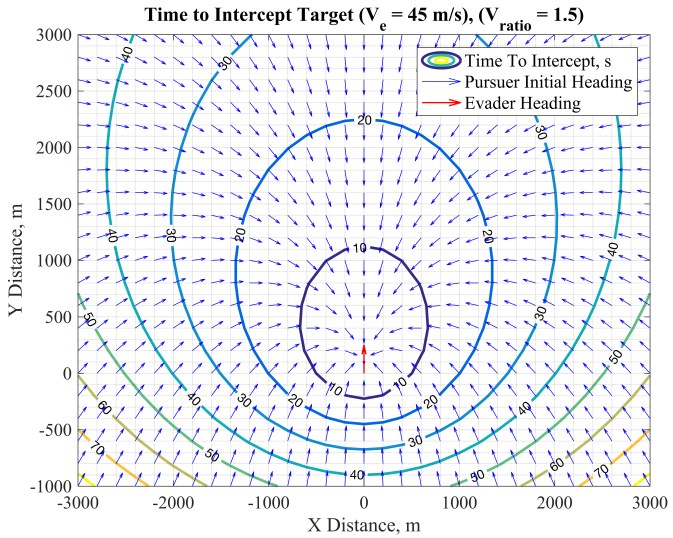

Figure 2: Kinematic solutions for time, heading, and position for direct evader interception. A speed ratio of 1.5 was used with an evader speed of $45\,\mathrm{m/s}$.

the pursuer whereas a subscript of e is for the evader) [34]. Then the maximum radius of curvature, ρ, of the pursuer was input into $\omega_p = \frac{v_p}{\rho}$ to determine the maximum turn rate ω_p [34].

Table 2: Simulation parameters that were used.

Simulation Parameter	**Value**	**Units**
Simulation Frequency	450	Hz
Tracking Update Frequency	10	Hz
Evader Speed	45	m/s
Evader Size	0.1	m
Pursuer G-Limit	5	g
Pursuer-Evader Speed Ratio	1.5	NA
Proportional Navigation Gain	3	NA

3.2.2 Proportional Navigation

The pursuer uses proportional navigation which relies on the angle between the evader's position and the pursuer's position. This angle is known as the line-of-sight (LOS) angle. The pursuer's position was assumed to be known perfectly in order to minimize proportional navigation error associated with the pursuer's position; only the evader's position error is considered. The objective of the proportional navigation law is to the keep the LOS angle constant when the evader does not turn (as shown in Figure 3) and to reduce the LOS rotation rate if the evader does turn [35]. During the simulation runtime, measurement error associated with the evader's position causes the LOS angle to change even when the true LOS may remain constant.

$$\frac{d\gamma}{dt} = N\frac{d\theta}{dt} \tag{3.1}$$

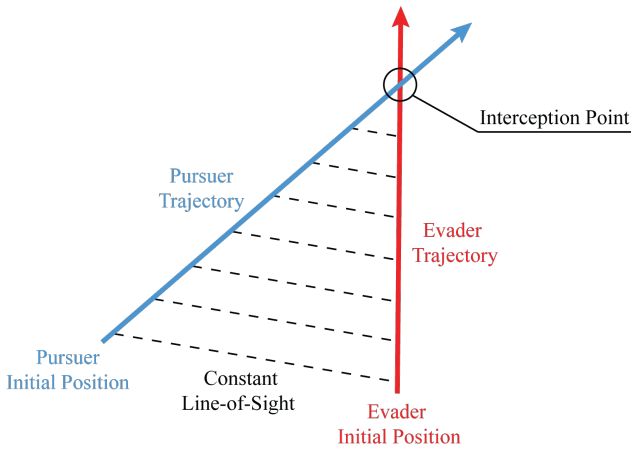

Figure 3: Proportional navigation with constant line-of-sight angles.

Eq. (3.1) is the proportional navigation equation. The pursuer's turn-rate, $\frac{d\gamma}{dt}$, is proportional to the LOS rotation rate $\frac{d\theta}{dt}$ [35]. The N term is the proportional navigation gain, which was equal to 3 for this simulation. Oftentimes, it is recommended to use a value between 3 and 5 (a value of 1 indicates a 1:1 turn-rate to LOS turn rate) [35]. In essence, Eq. (3.1) indicates that if the evader flies while turning away from the pursuer (LOS rate increases), then the turn rate will increase causing the pursuer to also turn but toward the evader. It is important to note that the pursuer does not necessarily fly directly at the evader; rather, the pursuer typically points along the projected path of the evader to keep the LOS angle constant [35].

3.2.3 Simulation Runtime

The simulation was designed to run in pseudo real-time at approximately $450\,\mathrm{Hz}$. This means that MATLAB® was run as fast as possible while the simulation loops depended on a constant change in an iterated time parameter. Throughout the simulation,

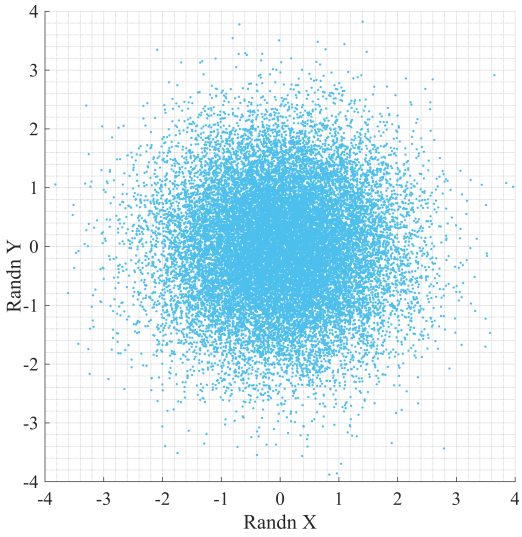

Figure 4: 2D noise distribution from the *randn* function from MATLAB®.

new evader position measurements are observed from the tracking sensor. This tracking sensor is setup to provide position measurements at a frequency of $10\,\mathrm{Hz}$. This means that for every $1\,\mathrm{s}$ in the simulation, the pursuer's and evader's position is incrementally moved 450 times. This also means that the pursuer receives a new position measurement of the evader 10 times during that $1\,\mathrm{s}$ interval. The $450\,\mathrm{Hz}$ is based on the approximated size of the evader $0.1\,\mathrm{m}$ which is divided by its speed $45\,\mathrm{m/s}$. The resultant value provides the amount of time required for the evader to move a body length away from its previous position. Although in the simulation the true position of the evader can be determined at any given instant from kinematics, the pursuer only uses the latest position measurement which creates a lag in the pursuit. Measurement updates for the evader follow a normally distributed noise function which has been used before in other simulations [36]. In order

to add noise to the evader's X-axis and Y-axis position, the tracking sensor's standard deviation was multiplied by a randomized value from a normal distribution. The 2D normal distribution is depicted in Figure 4.

The MATLAB® simulation is outlined as follows:

- **Step 1:** Initialize starting parameters (initial positions, tracking noise, KF enabled/disabled, iterations, etc).
- **Step 2:** Engagement iterations begin.
  - Calculate starting proportional navigation logic using measured/estimate evader position.
    - Calculate the line of sight angle (LOS).
    - Calculate the derivative of the line of sight angle ($\dot{LOS}$).
    - Multiply $\dot{LOS}$ with N (proportional navigation gain).
    - Compare commanded angular velocity term to maximum allowable turn rate based on G-limit.
    - Multiply angular velocity command by the change in simulation time.
  - If enabled, use KF to estimate the evader's next position (See Section 3.2.4).
  - Change pursuer heading based on PN.
  - Update position based on heading and speed for the evader and pursuer.
- **Step 3:** Repeat Step 3 until all iterations are complete (depends on number of test replicates).

- **Step 4:** Output results and store simulation data.

3.2.4 Kalman Filter Implementation

A random system process is assumed to be modeled as Eq. (3.2). Similarly, the measurement of the system process (oftentimes considered the observation) is described in Eq. (3.3). Both w_k and v_k are assumed to follow a white sequence and are made up of covariance structures (both independent of one another) [2].

$$x_{k+1} = \phi_k x_k + w_k \tag{3.2}$$

$$z_{k+1} = H_k x_k + v_k \tag{3.3}$$

The KF was used for this scenario since basic rectilinear kinematic models define the movements of the evader. The KF was run in the simulation loop every time a sensor measurement was updated. The discrete time KF model representation of the evading aircraft is represented in Eq. (3.4). The filter is broken down into the state transition matrix, ϕ_k, and the state variable vector, x_k. The dynamic models selected for Eq. (3.2) may incorporate an acceleration term; however, acceleration of the evader is $0\,\mathrm{m/s^2}$ in this scenario. The tracking sensor is assumed to provide noisy position estimates of the evader based on a prescribed measurement uncertainty. The measurement vector, z_k, and matrix which connects the measurement to the state matrix, H, are represented in Eqs. (3.5) and (3.6). Variables within the equations are representative of only the evader's parameters (i.e. x_e is indicative of the evader's X-axis position, etc.).

$$\begin{matrix} [x_{k+1}] & & [\phi_k] & & [x_k] \end{matrix}$$
$$\begin{bmatrix} (\mathbf{x}_e)_{k+1} \\ (\dot{\mathbf{x}}_e)_{k+1} \\ (\mathbf{y}_e)_{k+1} \\ (\dot{\mathbf{y}}_e)_{k+1} \end{bmatrix} = \begin{bmatrix} 1 & dt & 0 & 0 \\ 0 & 1 & 0 & 0 \\ 0 & 0 & 1 & dt \\ 0 & 0 & 0 & 1 \end{bmatrix} \begin{bmatrix} (\mathbf{x}_e)_k \\ (\dot{\mathbf{x}}_e)_k \\ (\mathbf{y}_e)_k \\ (\dot{\mathbf{y}}_e)_k \end{bmatrix} \tag{3.4}$$

$$z_k = \begin{bmatrix} x_e \\ y_e \end{bmatrix} \tag{3.5}$$

$$H = \begin{bmatrix} 1 & 0 & 0 & 0 \\ 0 & 0 & 1 & 0 \end{bmatrix} \tag{3.6}$$

The KF uses an error covariance matrix, P_k, which was initialized as shown in Eq. (3.7). P_k typically uses an a priori estimate of the states; however, the beginning of the pursuit scenario leading up to this endgame was assumed to initially use the tracking sensor's variance for each dynamic state. The process noise covariance, Q_k, and measurement noise covariance, R_k, are represented in Eqs. (3.8) and (3.9), respectively. Q_k makes up the covariance matrix defined by the white noise term, w_k. The process noise covariance matrix was tuned to 0.001. R_k makes up the measurement error covariance, v_k, as shown in Eq. (3.3). This measurement noise covariance matrix, R_k, is tuned based on a sensor's manufactured specifications where the variance of the tracking sensor was used. These covariance matrices define how trustworthy the dynamic models and sensors are based on a $95\,\%$ confidence interval. Q_k used values that were less than the values used in R_k, so the dynamic models were considered more trustworthy than the sensor measurements. In this scenario, the values within R_k and P_k were varied from 1^2m, 10^2m, 25^2m, and 50^2m as these four values make up the tracking sensor's variance levels.

$$P_k = \begin{bmatrix} \sigma^2 & 0 & 0 & 0 \\ 0 & \sigma^2 & 0 & 0 \\ 0 & 0 & \sigma^2 & 0 \\ 0 & 0 & 0 & \sigma^2 \end{bmatrix} \tag{3.7}$$

$$Q_k = \begin{bmatrix} 0.001 & 0 & 0 & 0 \\ 0 & 0.001 & 0 & 0 \\ 0 & 0 & 0.001 & 0 \\ 0 & 0 & 0 & 0.001 \end{bmatrix} \tag{3.8}$$

$$R_k = \begin{bmatrix} \sigma^2 & 0 \\ 0 & \sigma^2 \end{bmatrix} \tag{3.9}$$

The overall structure and process of the KF is as follows [2], which incorporates using the aforementioned matrices and variables:

1. Compute Kalman gain (Eq. (3.10)).

$$K_k = P_k^- H_k^T (H_k P_k^- H_k^T + R_k)^{-1} \tag{3.10}$$

2. Correct/update estimates with measurements (Eq. (3.11)).

$$\hat{x}_k = \hat{x}_k^- + K_k(z_k - H_k \hat{x}_k^-) \tag{3.11}$$

3. Calculate the error covariance for the updated estimate (Eq. (3.12)).

$$P_k = (I - K_k H_k) P_k^- \tag{3.12}$$

4. Propagate/project estimates (Eqs. (3.13) and (3.14)).

$$\hat{x}_{k+1}^- = \phi_k \hat{x}_k \tag{3.13}$$

$$P_{k+1}^- = \phi_k P_k \phi_k^T + Q_k \tag{3.14}$$

It should be noted that the superscript minus $(^-)$ indicates that the variable is from the previous time step. Once the latest update is determined the superscript minus disappears as shown in Eq. (3.11). The I that is shown in Eq. (3.12) is an identity matrix which depends on the number of states ($n \times n$) where this experiment used Eq. (3.15). The KF assumed initial values for each of the states, which were changed at each KF time step. The evader was assumed to start at the origin or *(0,0)*. The velocity components were assumed to be close to the true values since the simulation was setup to focus on an endgame; thus, the initial estimates for the X-axis and Y-axis velocity components were $0\,\mathrm{m/s}$ and $40\,\mathrm{m/s}$, respectively. These estimates were all updated at $10\,\mathrm{Hz}$.

$$I = \begin{bmatrix} 1 & 0 & 0 & 0 \\ 0 & 1 & 0 & 0 \\ 0 & 0 & 1 & 0 \\ 0 & 0 & 0 & 1 \end{bmatrix} \tag{3.15}$$

3.2.5 Simulation Analysis

Miss distance is the basis of comparison for the non-KF and KF estimation methods and also included time of miss distance. The miss distance value is determined using the first local minimum of each engagement, which is found from taking the change in the Euclidean distance between the true evader position and the pursuer position. Once a sign change occurs, the miss distance is found. The non-KF method is assessed first based on miss distance while only using raw tracking sensor measurements. Next the miss distance from the KF estimation method will be evaluated. Each method will then be compared to evaluate the impact of varying tracking sensor uncertainty on miss distance and time of

miss distance. The comparative analysis will include miss distance comparisons between median and range along with the mean miss distance. Each of the five starting positions are run 100 times using four tracking sensor uncertainties. This means that there are a total of 2000 engagements per estimation method.

3.3 Simulation Results and Discussion

3.3.1 Engagements Without a Kalman Filter

Figure 5 shows the variation in the minimum miss distance due to the tracking measurement uncertainty ($\sigma_{tracking} = 50m$). Figure 6 is an example of one of the 100 iterations from this starting position with $\sigma_{tracking} = 50m$. This engagement ran for $40\,\mathrm{s}$ allowing the pursuer to attempt multiple interceptions.

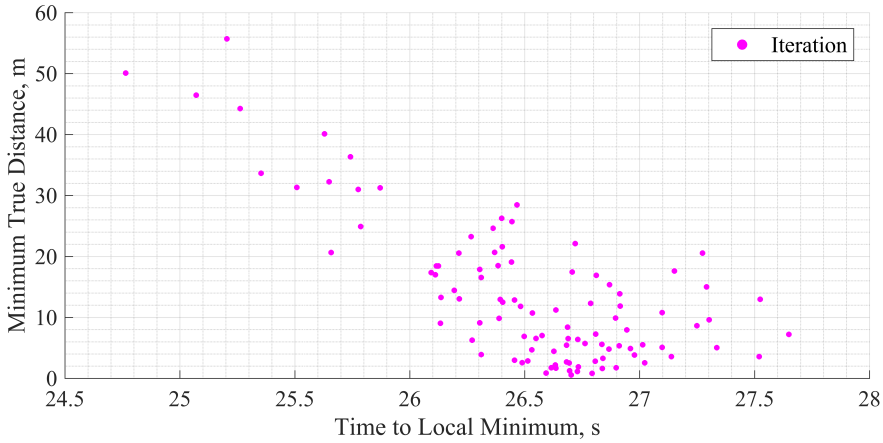

Figure 5: Miss distance vs time of occurrence for 100 iterations of $45°$ pursuer starting heading with a tracking standard deviation of $50\,\mathrm{m}$.

When considering the same starting condition while varying the tracking measurement uncertainty, the increased measurement uncertainty greatly impacted the pursuer's

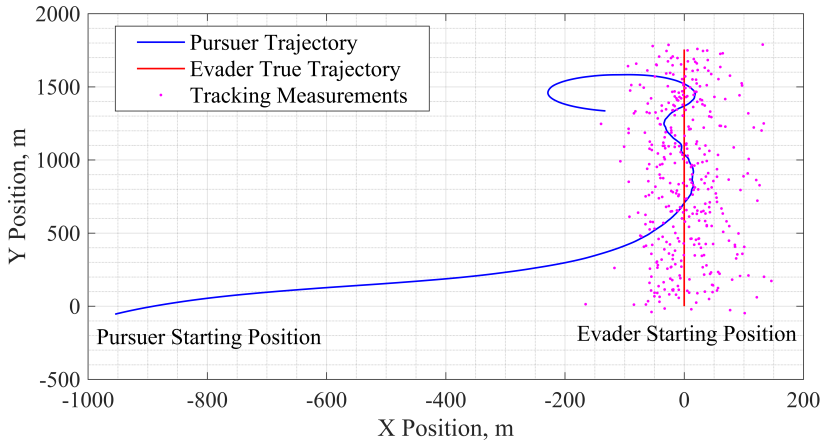

Figure 6: Representative ground track with $45°$ pursuer starting heading with a tracking standard deviation of 50 m.

miss distance. This effect is observed by looking at the $315°$ representative engagements where the tracking noise uncertainty was increased Figures 7a to 7d. The magenta dots indicate the measured evader's position and are bounded by $2\sigma_{tracking}$. As expected, by decreasing the measurement uncertainty, the evader's position measurements approach the true evader position.

3.3.2 Engagements With a Kalman Filter

When incorporating the KF in this simulation, the algorithm was run in pseudo real-time to provide the pursuer with updated evader position estimates. Figure 8 provides the ground track for the pursuing aircraft, KF position estimates for the evader, and the raw tracking measurements that were used in the KF. Similar to what was shown in Figure 7, the tracking uncertainty was varied, which shows the position measurements

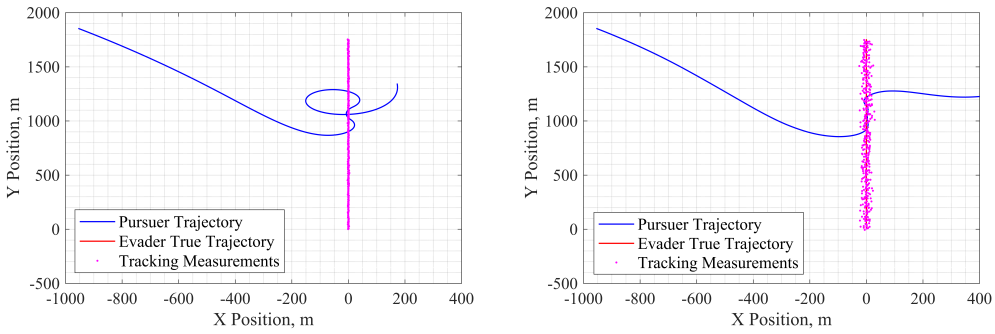

(a) Ground track with $\sigma_{tracking} = 1m$.

(b) Ground track with $\sigma_{tracking} = 10m$.

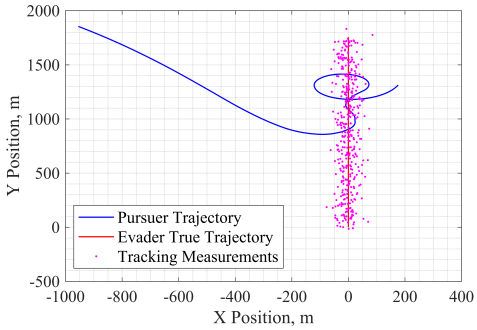

(c) Ground track with $\sigma_{tracking} = 25m$.

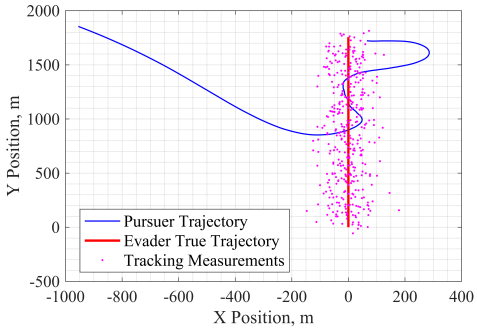

(d) Ground track with $\sigma_{tracking} = 50m$.

Figure 7: $315°$ initial heading engagement while varying tracking measurement noise without a Kalman Filter.

approaching the true position of the evader when uncertainty decreases. The KF estimation resulted in a more defined trajectory for the evading aircraft (Figure 8). It should be noted that the pursuer maneuvered into a left turn as soon as the first intercept occurred. The engagements were allowed to run beyond the initial interception up until $40\,\mathrm{s}$.

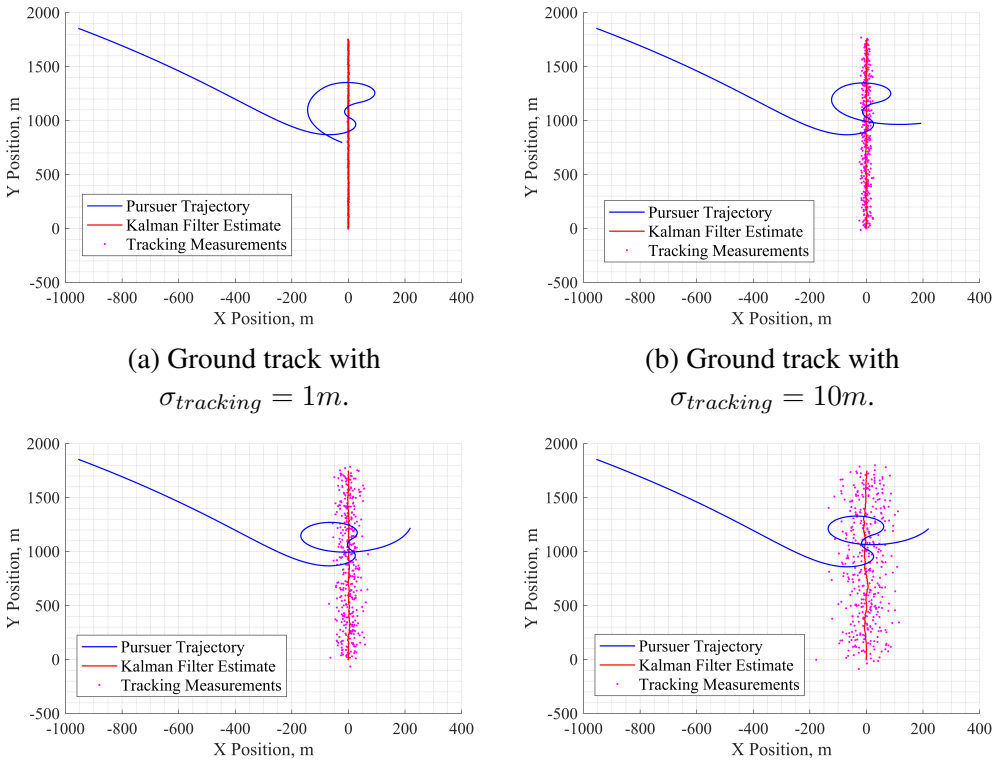

(a) Ground track with $\sigma_{tracking} = 1m.$

(b) Ground track with $\sigma_{tracking} = 10m.$

(c) Ground track with $\sigma_{tracking} = 25m.$

(d) Ground track with $\sigma_{tracking} = 50m.$

Figure 8: $315°$ initial heading engagement while varying tracking measurement noise with a Kalman Filter.

One major advantage of using a KF was the ability to estimate states with improved uncertainty bounds and without a sensor directly measuring each state variable. In this scenario, the same tracking sensor uncertainty values from the non-KF engagements

were used. When using the KF, position was estimated along with velocity. In the previous non-KF approach, velocity could only be determined through position differentiation. Differentiated velocity would then be subjected to position error along with propagation error due to the differentiation method. From the bottom subfigure in Figure 9, the method of differentiation resulted in large magnitudes for the estimated speed which is unrealistic based on the known capabilities of the evader. The top subfigure in Figure 9 depicts the speed components estimated from using the KF and the $95\,\%$ confidence interval for each estimate. The evader's component speeds showed improvements over time eventually converging near the true values.

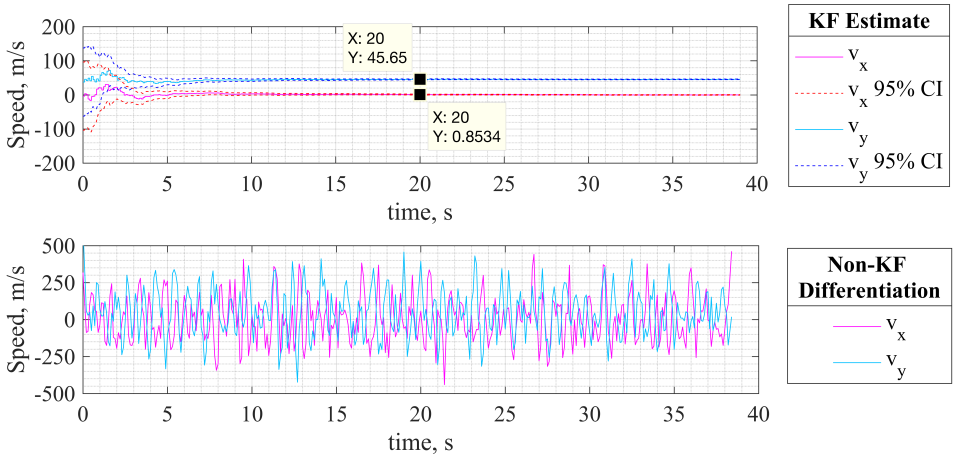

Figure 9: Evader speed components versus time for both KF estimation and non-KF differentiation during the $0°$ initial heading engagement ($\sigma = 50m$).

Similar to the velocity convergence that is seen from using a KF, Figure 10 shows the position convergence for the evader when using the KF. This particular engagement suffers from a large initial uncertainty since the tracking measurement standard deviation was $50\,\mathrm{m}$. The large standard deviation results in large error uncertainty bounds, shown

in green, during the start of the engagement; however, the uncertainty bounds decrease as position estimates from the KF improve over time. As expected, the $95\,\%$ confidence interval for position contains the true position of the evader which follows along the Y-axis. Although the tracking sensor uncertainty bounds without a KF includes the true position of the evader, the uncertainty bounds remain constant over time which provides poor position estimates for the evader.

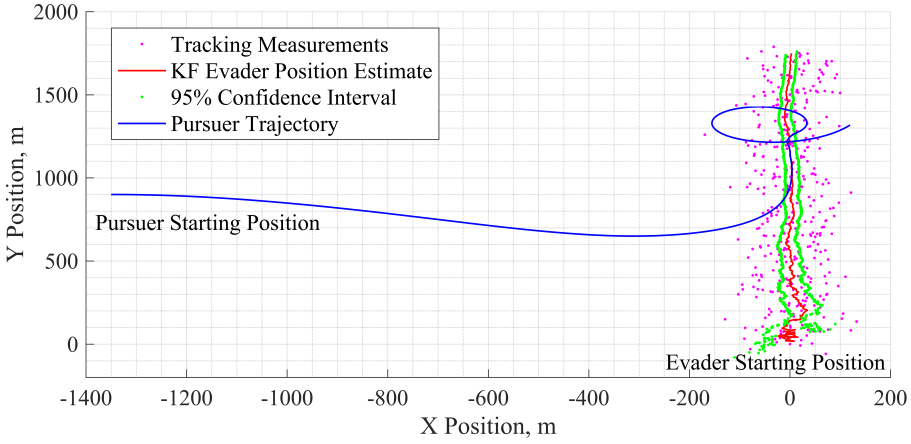

Figure 10: Ground track plot of the pursuer and evader position estimates from the KF during the $0°$ initial heading engagement ($\sigma = 50m$). Estimated evader position also includes the $95\,\%$ confidence interval which is shown in green.

The error state covariance matrix P_k was evaluated for each tracking sensor uncertainty level and showed improvements in the state estimate uncertainty for each KF state. The values within P_k were initially based on the tracking sensor's uncertainty; however, the values were corrected and updated at every KF time step. Figure 11 depicts the P_k values for position and velocity (x and y position and velocity estimates experienced the same uncertainty) versus time during the $45°$ engagement. The initial covariance estimate for

each uncertainty level is shown by the dotted lines. These values are also representative of the constant tracking sensor uncertainty that is used in the non-KF method. The error state covariance decreased throughout the engagements which is indicative of a decrease in the $95\,\%$ confidence interval range for the state estimates. When looking at Figure 11, the $100\,\mathrm{m}$ position uncertainty reduced by half within $1\,\mathrm{s}$. Furthermore, the $100\,\mathrm{m}$ position uncertainty reduced to $20\,\mathrm{m}$ uncertainty after about $10\,\mathrm{s}$. The velocity error state covariance estimates decreased more than the position error estimates, which may be due to not having velocity sensor measurements. The position results are significant as the KF with the largest tracking sensor uncertainty becomes equivalent to using a better tracking sensor. Figure 12 shows the representative distribution of uncertainty during the $45°$ engagements. The X-axis is separated by the four uncertainty levels and the Y-axis is the KF position state estimate uncertainty throughout the entire simulation runtime ($40\,\mathrm{s}$). This box plot provides data associated with the spread of the data shown in Figure 11 where the centerline in each box is the median and is framed by the 25th and 75th percentile. The outliers are indicated with red $+$ signs. Over the entire $40\,\mathrm{s}$ runtime, the mean uncertainty from the KF reduced by more than half, which indicates improvement in the evader's position uncertainty when using a KF.

3.3.3 Engagement Comparisons With and Without a Kalman Filter

Comparisons between the KF method and non-KF estimation method are now directly presented. When considering a decrease in tracking noise standard deviation ($Uncertainty = \pm\, 2\sigma$), the miss distance reduced in most cases as shown in Figures 13

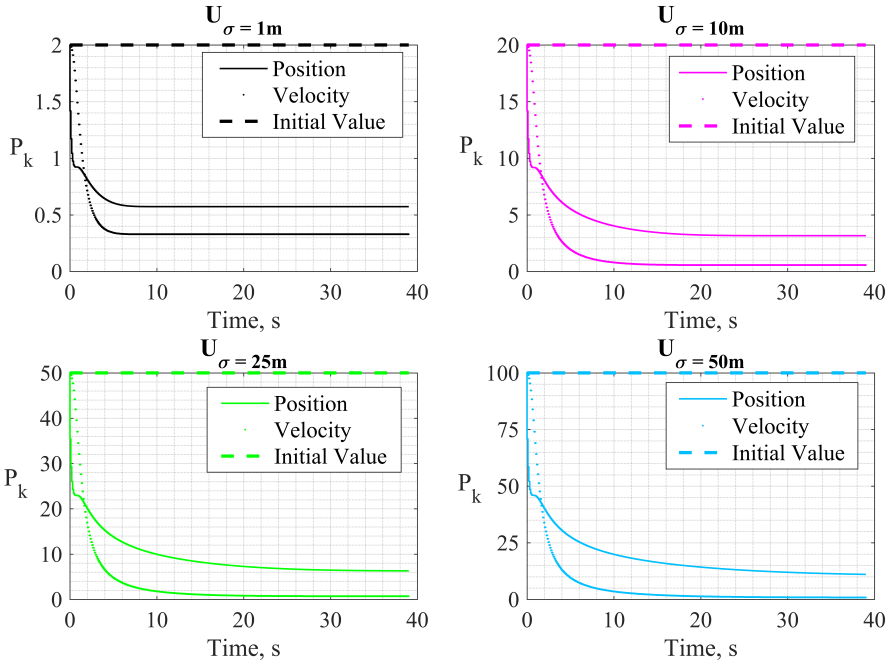

Figure 11: Error state covariance values for position and velocity compared to initial error state estimates during the $45°$ initial heading engagement.

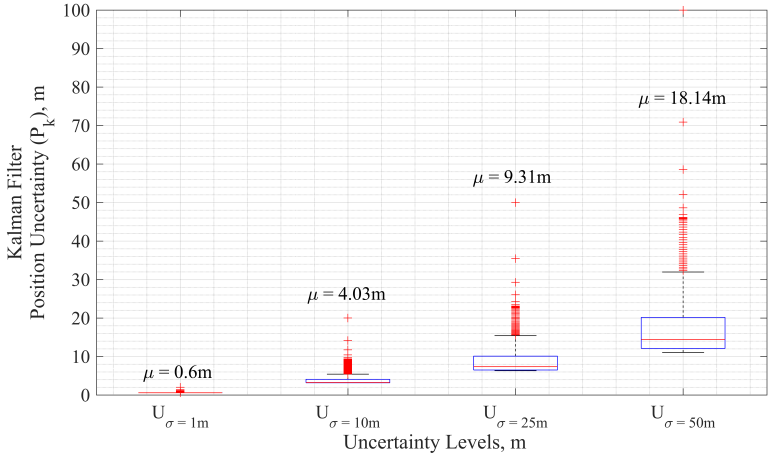

Figure 12: Kalman Filter position estimate uncertainty versus baseline uncertainty value during the $45°$ initial heading engagement.

to 17. Each plot was constructed through MATLAB® using [37]. It is important to note that each boxplot is representative of 100 replicates. Mean miss distance increased with an increase in tracking measurement uncertainty (shown as standard deviation) in most cases. The miss distance range for the 100 replicates were reduced when using a KF. Figure 17 shows the non-KF miss distance with $\sigma = 50m$ that has a median miss distance that is much larger than all of the other engagements. Although that median miss distance is expected to be greater than the medians which experienced less tracking sensor uncertainty, the median value was close to $80\,\mathrm{m}$ whereas the other $\sigma = 50m$ engagements were closer to $10\,\mathrm{m}$. Similarly, the $315°$ (Figure 17) engagement resulted in an unexpected decrease in the median with an increase in measurement standard deviation when using a KF. The $270°$ engagement, shown in Figure 16, resulted in miss distance similarities when comparing the non-KF method to the KF estimation method. These miss distance results were expected to be similar to the $90°$ engagement (Figure 14) since both engagements experienced more X-axis position error than Y-axis position error due to the pursuer starting in front and behind the evader; however, this result was not observed. The result may be due to the amount of time that the pursuer spends inside of the measurement uncertainty area around the evader. The head-on $270°$ engagement limits the amount of time inside of the uncertainty area since the evader moves directly at the pursuer. The trailing $90°$ engagement experiences the tracking uncertainty area for a longer duration since the evader and pursuer move in the same direction. This phenomenon can also be described in terms of the relative velocity of the evader, as the relative velocity is greater in the head-on engagement than in the trailing engagement.

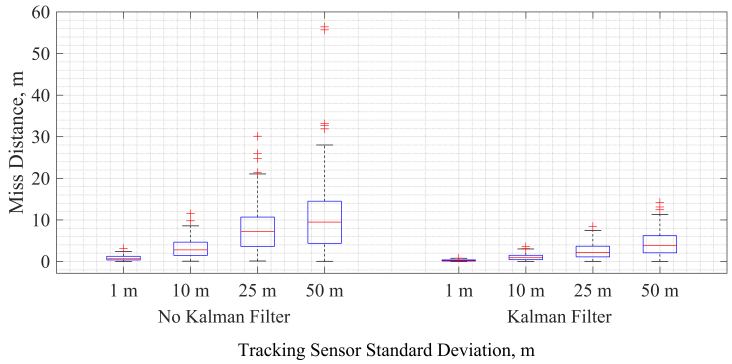

Figure 13: Comparative miss distance boxplot for the $45°$ pursuer starting heading.

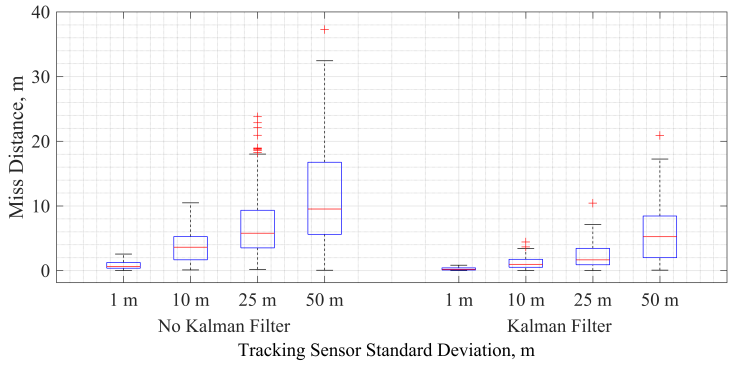

Figure 14: Comparative miss distance boxplot for the $90°$ pursuer starting heading.

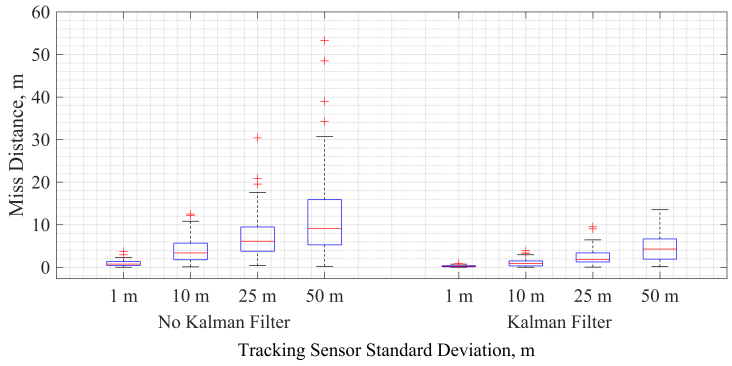

Figure 15: Comparative miss distance boxplot for the $0°$ pursuer starting heading.

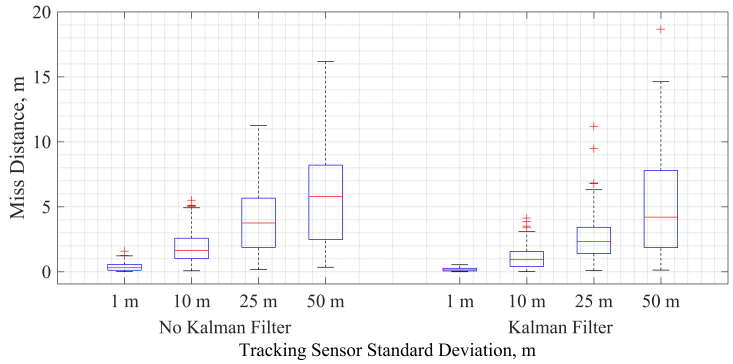

Figure 16: Comparative miss distance boxplot for the 270° pursuer starting heading.

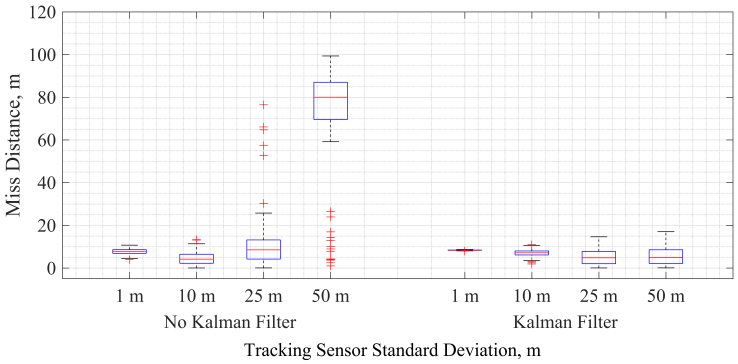

Figure 17: Comparative miss distance boxplot for the 315° pursuer starting heading.

Table 3 provides mean miss distance and time data for all of the engagement results. It is important to remember that each mean miss distance is representative of 100 iterations for that initial starting condition along with the respective tracking sensor uncertainty condition. The engagements where the pursuer started with a heading of $270°$ and $90°$ led to minimal path deviations resulting in achieving miss distances close to the expected $20\,\mathrm{s}$. This phenomenon may be explained as these two engagements are affected more from X-axis position measurement error due to starting directly behind and ahead of the evader. Although there may be some effect from Y-axis position error through minor path deviations, the Y-axis position error is minimal compared to X-axis position error.

Table 3: Simulation results with the Kalman Filter disabled and enabled (data separated by tracking sensor standard deviation).

State Estimator	**Initial Heading**	**Mean Miss Distance, m**				**Mean Intercept Time, s**			
		$1\,\mathrm{m}$	$10\,\mathrm{m}$	$25\,\mathrm{m}$	$50\,\mathrm{m}$	$1\,\mathrm{m}$	$10\,\mathrm{m}$	$25\,\mathrm{m}$	$50\,\mathrm{m}$
Non-Kalman Filter	$0°$	0.92	3.99	7.18	11.79	26.78	27.81	28.06	28.20
	$45°$	0.87	3.36	7.86	11.47	25.92	26.47	26.51	26.64
	$90°$	0.82	3.78	7.43	11.82	20.00	20.01	20.00	20.05
	$270°$	0.39	1.86	4.01	5.78	20.00	20.00	20.00	20.00
	$315°$	7.67	4.64	11.63	71.27	23.37	23.98	24.37	21.65
Kalman Filter	$0°$	0.26	1.06	2.35	4.65	26.76	26.77	26.89	27.15
	$45°$	0.25	1.06	2.61	4.43	25.90	25.91	25.98	26.12
	$90°$	0.26	1.19	2.25	5.91	20.00	20.00	20.01	20.02
	$270°$	0.17	1.09	2.74	4.98	20.00	20.00	20.00	20.00
	$315°$	8.32	6.95	4.86	5.67	23.26	23.28	23.38	23.42

Percentage change was considered in this scenario since each engagement was tested without a KF and then with a KF (Table 4). Positive values are indicative of the mean miss distance from KF estimation being greater than values from the non-KF

method. The negative percentage change indicates that the mean miss distance when using the KF was less than the miss distance without using a KF. In every engagement, except $315°$ with $\sigma = 1m$ and $\sigma = 10m$, the KF resulted in improved miss distances. This result may be due to uncertainty having minimal impact on the engagement. The maximum percentage change between non-KF and KF was approximately $92.04\,\%$ (KF improved miss distance), where the largest change in the mean miss distance was approximately $65.6\,\mathrm{m}$. This result is significant since a successful miss distance may be defined as having the pursuer achieve a miss distance within a certain threshold.

Table 4: Percentage change based on miss distance with and without a KF.

Miss Distance Difference (Percent Change)

Initial Heading	Tracking Measurement Standard Deviation $U_{\sigma=1m}$	$U_{\sigma=10m}$	$U_{\sigma=25m}$	$U_{\sigma=50m}$
$0°$	$-0.66\,\mathrm{m}$ ($-58.06\,\%$)	$-2.93\,\mathrm{m}$ ($-73.43\,\%$)	$-4.83\,\mathrm{m}$ ($-67.27\,\%$)	$-7.14\,\mathrm{m}$ ($-60.56\,\%$)
$45°$	$-0.62\,\mathrm{m}$ ($-71.26\,\%$)	$-2.30\,\mathrm{m}$ ($-68.45\,\%$)	$-5.25\,\mathrm{m}$ ($-66.79\,\%$)	$-7.04\,\mathrm{m}$ ($-61.38\,\%$)
$90°$	$-0.56\,\mathrm{m}$ ($-68.29\,\%$)	$-2.59\,\mathrm{m}$ ($-68.52\,\%$)	$-5.18\,\mathrm{m}$ ($-69.72\,\%$)	$-5.91\,\mathrm{m}$ ($-50.00\,\%$)
$270°$	$-0.22\,\mathrm{m}$ ($-56.41\,\%$)	$-0.77\,\mathrm{m}$ ($-41.40\,\%$)	$-1.27\,\mathrm{m}$ ($-31.67\,\%$)	$-0.8\,\mathrm{m}$ ($-13.84\,\%$)
$315°$	$+0.65\,\mathrm{m}$ ($+8.47\,\%$)	$+2.31\,\mathrm{m}$ ($+49.78\,\%$)	$-6.77\,\mathrm{m}$ ($-58.21\,\%$)	$-65.6\,\mathrm{m}$ ($-92.04\,\%$)

3.4 Conclusion

The first experiment considered a pursuer-evader simulation which varied tracking sensor uncertainty along with initial pursuer position and heading conditions. A non-KF method and KF estimation method were introduced and used to evaluate the performance

of a pursuer during multiple engagement iterations. In general, an increase in tracking sensor uncertainty resulted in an increase in the miss distance for the pursuer. Similarly, when considering 100 replicates for an initial starting condition and uncertainty level, the KF reduced the range of miss distances in most cases. When comparing the use of a KF with using only raw tracking sensor measurements, the KF improved the miss distance results by more than $50\,\%$ in most engagements. The KF resulted in improved position uncertainty compared to using only raw tracking sensor measurements with fixed uncertainty. Throughout the engagements, the KF provided more accurate positions for the evader as opposed to just using the raw tracking-based measurements. The KF also resulted in expanding the modeling capabilities of the evader through estimating the evader's velocity.

CHAPTER 4

ASSESSMENT OF FIXED-WING UAV SYSTEM IDENTIFICATION MODELS DURING ACTUATOR AND PAYLOAD DROP FAILURES

This chapter details an experiment in which an aircraft experiences free-flight failures. This experiment implements an Extended Kalman Filter coupled with inexpensive sensors. Aircraft states along with the stability and control derivatives were estimated using an EKF. The dynamic models came from the lateral-directional and longitudinal linearized equations of motion. The estimates of the aforementioned parameters were assessed before and after free-flight failures occurred. The aircraft experienced aileron control surface failures which are related to loss of control effectiveness; similarly, the aircraft experienced aerial delivery failures where a payload failed to release from the center of gravity bay and wing bay.

This conference paper was initially published in AIAA SciTech 2021 and was included within this thesis with some minor changes [38].

4.1 Introduction

Companies around the world, such as Zipline, have been developing unmanned aerial vehicles (UAVs) that specialize in delivery of medical supplies [39]. By using autonomous fixed-wing drones, delivery is within minutes and eliminates potential human-to-human exposure; both are critical needs of medical centers as illustrated by the COVID-19 pandemic [40]. Despite these benefits, drone delivery remains contentious as aircraft

failures may cause property and personal damages [41]. Flight failures consisting of fixed-position control surfaces and payload mechanisms are a cause for concern as these types of failures can lead to anomalous aircraft behavior and inoperable UAVs. Thus, a need exists to assess aircraft dynamics during free-flight failures in order to develop fault mitigation strategies. These strategies are particularly important for fixed-wing and VTOL payload deployment failures as this new field has been minimally investigated. System identification approaches may be used to identify the type of failure and severity while adjusting model coefficients, biases, and state estimates for the aircraft. The aircraft states and dynamic models may then be used for adaptive control schemes to aid in mitigating failure effects; however, these control schemes are not addressed in this work. An Extended Kalman Filter (EKF) was applied to these failures as it provides a means of expanding the modeling capabilities of the aircraft.

In this study, fixed-wing failure scenarios were assessed using system identification. Three orthogonal multi-sine input signals were used on the roll, pitch, and yaw axes in conjunction with an EKF to determine state and aerodynamic coefficient estimates. The fixed-wing aircraft was flown manually during actuator and payload failure scenarios with reduced instrumentation (no onboard differential pressure sensor and pitot tube). The main purpose of this study was to identify changes in the dynamic models of the aircraft during failure scenarios using an EKF; accuracy assessments of the estimated stability and control coefficients was considered a secondary purpose as these parameters provide insight on the aircraft's flight performance. Assessing and identifying failures is integral to the development of fault mitigating flight controllers for fixed-wing and VTOL UAVs.

4.2 Aircraft Design

4.2.1 E-Flite Turbo Timber

The E-Flite Turbo Timber aircraft (referred to as Timber hereafter) is a short take-off and landing fixed-wing UAV that features two ailerons, one elevator, and a rudder. Additionally, the Timber has controllable flaps but were only used on landing approaches. A Hex Cube Black flight controller paired with the open source software suite, PX4, was used for all flight testing [42]. Positional data was collected using a Here2 GPS receiver to provide flight trajectory monitoring. Telemetry was coupled with radio control (RC) through the RFD 900x air unit and the RFDesign TXMOD, which is an add-on to the FrSky Taranis Q X7 controller. The ground station, QGroundControl, was linked through the RFDesign TXMOD WiFi which enabled real-time software parameter changes during flight tests. The flight controller and control hardware was stored inside of the Timber's fuselage (Figure 18). An inexpensive angle of attack (AOA) sensor, made from a low-cost hall effect sensor and carbon fiber rod, was mounted near the left wing tip and was designed similarly to the AOA sensors used in wind tunnel studies [43]. Timber measurements are in Table 5, where the moment of inertia was determined through SOLIDWORKS® modeling. The Timber parameters were used as constant values in the EKF and input into Athena Vortex Lattice (AVL) for aerodynamic modeling (aerodynamic modeling will be discussed in Section 4.3.1).

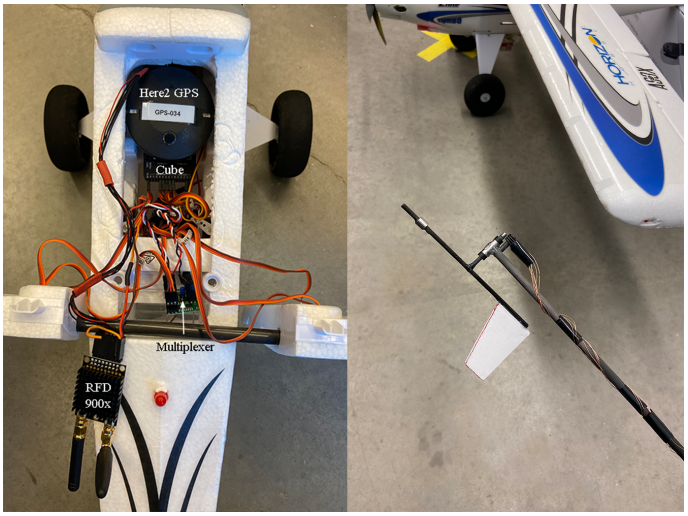

Figure 18: E-Flite Turbo Timber hardware internals and angle of attack sensor.

Table 5: E-Flite Turbo Timber parameters (mass and moment of inertia changed depending on the payload configuration).

Parameter	Minimum	Maximum	Units
UAV Mass (m_{uav})	1.90	2.78	kg
Moment of Inertia (I_x)	0.0642	0.0697	$kg * m^2$
Moment of Inertia (I_y)	0.1042	0.1227	$kg * m^2$
Moment of Inertia (I_z)	0.1511	0.1698	$kg * m^2$
Payload Mass ($m_{payload}$)	0.160		kg
Drop Mechanism Mass (m_{drop})	0.280		kg
Wingspan (b)	1.5462		m
Average Wing Chord ($\bar{c}$)	0.2159		m
Wing Area (S)	0.3338		m^2
AOA Sensor Location from CG (x_a)	0.2794		m
AOA Sensor Location from CG (y_a)	-0.7493		m

4.2.2 Control Surface Failure Setup

Fixed-wing UAVs and VTOL aircraft use servo actuators to deflect control surfaces, changing the aircraft's orientation and/or attitude. The Timber uses six servo actuators: two servos for the flaps, two for the ailerons, one for the elevator, and one servo for the rudder. During control surface failure testing, the left aileron was subjected to fixed-position failures resulting in the right aileron having sole control of the roll axis. Fixed-position failures occur when a control surface deflects to a certain angular position and remains fixed regardless of pilot input or flight controller output. During left aileron fixed-position failures, the right aileron was required to counteract the adverse moment while superimposing additional right aileron deflection resulting in reduced roll control and effectiveness. For example, a left aileron with a fixed-position failure equal to -20° (negative roll moment) requires the right aileron to be positioned equal to 20° (positive roll moment) to counteract the adverse roll moment. Thereafter, a desired rolling maneuver requires the right aileron to deflect more or less than 20°. If the left aileron's trailing edge points upward along the negative Z-axis, then a negative roll moment is produced; thus, the left aileron's deflection angle is denoted as negative. Likewise, if a left aileron's trailing edge points downward along the Z-axis (positive deflection angle), a positive roll moment is produced.

Aileron failures utilized a multiplexer connected to two auxiliary pulse-width modulation (PWM) outputs from the Cube flight controller. One auxiliary output sends the failure PWM signal and the other auxiliary output sends a switch signal (Figure 19). The PX4 aileron channel is connected to the first main input in the multiplexer to provide

nominal control, and the main output channel from the multiplexer is connected directly to the servo actuator, which is used to deflect the control surface. If the switch signal changes from a low PWM value to high PWM value, the multiplexer will switch from the nominal PWM signal to the failure PWM signal. The failure can be disabled by changing the switch signal back to a low PWM value. The failure PWM signals were modified by the FrSky Taranis Q X7 controller which resulted in different fixed-position deflection angles.

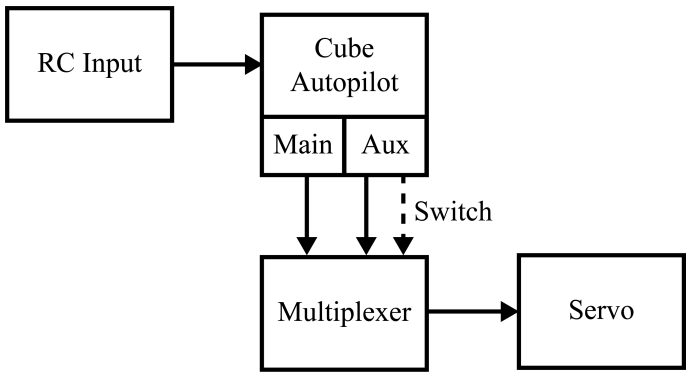

Figure 19: Multiplexer PWM wiring diagram for servo failure condition.

4.2.3 Payload Drop Failures

Two different payload drop failure configurations were used during free-flight. The first configuration consists of a center of gravity (CG) payload release where the payload's parachute fails to deploy and entangles on the drop mechanism (Figure 20a). The other variation of this failure utilizes a bay release compartment where the parachute entangles within the fuselage. The second failure scenario entails a wing-based configuration where a payload's parachute is released while the payload remains attached to

the wing (Figure 20b). Each of the payload failures uses electromagnets to release the payloads and a failsafe pin release mechanism to terminate the failure tests (Figure 21).

(a) Center of gravity payload release failure.

(b) Wing bay payload release failure.

Figure 20: Photos of the aircraft in free-flight experiencing arial delivery failures.

4.3 Methodology

4.3.1 Aircraft Dynamics

The Timber dynamic model was based on the body-fixed coordinate frame (Figure 22). The control surface deflections are positive depending on the moment that is produced. The rudder is considered positive when the trailing edge is deflected to the right along the Y-axis, creating a positive yaw moment. A positive elevator deflection occurs when the trailing edge is deflected upward along the Z-axis, resulting in a positive pitching moment. The left and right aileron deflections are always opposite; for instance, the trailing edge of the right aileron is deflected upward whereas the trailing edge of the

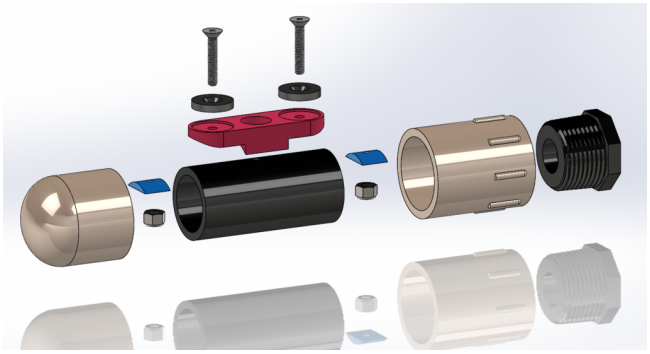

(a) Exploded-view of the payload.

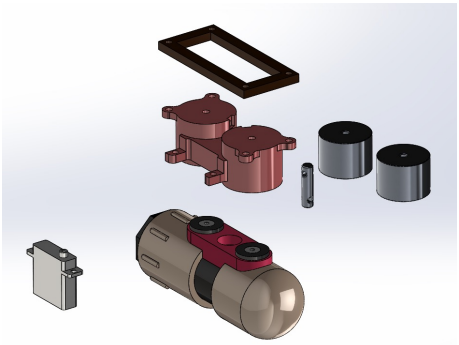

(b) Exploded-view of the payload drop mechanism (without fasteners) along with a fully assembled payload.

Figure 21: Rendered photos of the payload and drop mechanism assemblies.

left aileron is downward for a given roll command. A positive roll moment is produced when the right aileron's trailing edge deflects upward and the left aileron's trailing edge deflects downward.

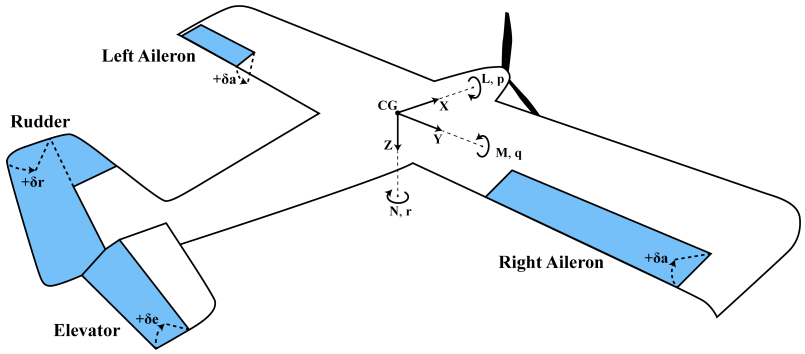

Figure 22: E-Flite Turbo Timber body-fixed coordinate frame (control surfaces highlighted in blue).

The Timber's forces and moments are described by Eqs. (4.1) and (4.2), where aerodynamic forces (X, Y, and Z) and moments (L, M, and N) are separated [44]. The Z force component will be put in terms of lift, L, and the aerodynamic moments

(L, M, and N) will be denoted as lowercase characters (l, m, and n) for readability. It is important to note that the dimensional forces and moments are equal to a respective dimensionless coefficient ($C_{component}$) along with dimensional aircraft and flight parameters. $\bar{q}$ represents the dynamic pressure (Eq. (4.3)), S is the wing area, b is the wingspan, and $\bar{c}$ represents the mean wing chord. The dynamic pressure equation includes air density, ρ, and velocity, v.

$$\begin{aligned} X &= C_x \bar{q} S \\ Y &= C_y \bar{q} S \\ Z &= C_z \bar{q} S \end{aligned} \tag{4.1}$$

$$\begin{aligned} L &= C_l \bar{q} S b \\ M &= C_m \bar{q} S \bar{c} \\ N &= C_n \bar{q} S b \end{aligned} \tag{4.2}$$

$$\bar{q} = \frac{1}{2} \rho v^2 \tag{4.3}$$

The aerodynamic forces and moments can be expressed in state-space form where the lateral-directional and longitudinal equations of motion are considered decoupled (Eqs. (4.4) and (4.5)). The dynamics assume small perturbation theory which linearizes the aircraft's equations of motion [44]. The lateral-directional equations of motion use forces and moment derivations with respect to the β, p, r, and ϕ states along with the control deflection parameters, δa and δr. Short-period approximation was assumed for the longitudinal dynamics, where the forces and moments were derived with respect

to α, q, and δe. Short-period assumes constant airspeed along with fast aircraft responses in the longitudinal dynamics [45].

$$\begin{bmatrix} \Delta\dot{\beta} \\ \Delta\dot{p} \\ \Delta\dot{r} \\ \Delta\dot{\phi} \end{bmatrix} = \begin{bmatrix} \frac{Y_\beta}{v_0} & \frac{Y_p}{v_0} & -(1-\frac{Y_r}{v_0}) & \frac{g\cos\theta_0}{v_0} \\ l_\beta & l_p & l_r & 0 \\ n_\beta & n_p & n_r & 0 \\ 0 & 1 & 0 & 0 \end{bmatrix} \begin{bmatrix} \Delta\beta \\ \Delta p \\ \Delta r \\ \Delta\phi \end{bmatrix} + \begin{bmatrix} 0 & \frac{Y_{\delta_r}}{v_0} \\ l_{\delta_a} & l_{\delta_r} \\ n_{\delta_a} & n_{\delta_r} \\ 0 & 0 \end{bmatrix} \begin{bmatrix} \Delta\delta_a \\ \Delta\delta_r \end{bmatrix} \tag{4.4}$$

$$\begin{bmatrix} \Delta\dot{\alpha} \\ \Delta\dot{q} \end{bmatrix} = \begin{bmatrix} \frac{Z_\alpha}{v_0} & 1+\frac{Z_q}{v_0} \\ m_\alpha & m_q \end{bmatrix} \begin{bmatrix} \Delta\alpha \\ \Delta q \end{bmatrix} + \begin{bmatrix} \frac{Z_{\delta_e}}{v_0} \\ m_{\delta_e} \end{bmatrix} \begin{bmatrix} \Delta\delta_e \end{bmatrix} \tag{4.5}$$

The dimensional characteristics of the aircraft along with the dimensionless coefficients can be substituted into the Timber's state-space lateral-directional and longitudinal equations (Eqs. (4.6) and (4.7)). Bias terms were also added onto the state-space models to account for the aircraft's inability to obtain and account for perfect trim conditions during flight [19]. Similarly, the bias terms account for any error or model deviations which may have accumulated from added noise during free-flight testing. The state-space models were directly input into the EKF state transition matrix but will be explained in Section 4.3.3.

$$\begin{bmatrix} \Delta\dot{\beta} \\ \Delta\dot{p} \\ \Delta\dot{r} \\ \Delta\dot{\phi} \end{bmatrix} = \begin{bmatrix} \frac{\bar{q}S}{mv_0}C_{Y_\beta} & \frac{\bar{q}Sb}{2mv_0^2}C_{Y_p} & -(1-\frac{\bar{q}Sb}{2mv_0^2}C_{Y_r}) & \frac{g\cos\theta_0}{v_0} \\ \frac{\bar{q}Sb}{I_x}C_{l_\beta} & \frac{\bar{q}Sb^2}{2I_xv_0}C_{l_p} & \frac{\bar{q}Sb^2}{2I_xv_0}C_{l_r} & 0 \\ \frac{\bar{q}Sb}{I_z}C_{n_\beta} & \frac{\bar{q}Sb^2}{2I_zv_0}C_{n_p} & \frac{\bar{q}Sb^2}{2I_zv_0}C_{n_r} & 0 \\ 0 & 1 & 0 & 0 \end{bmatrix} \begin{bmatrix} \Delta\beta \\ \Delta p \\ \Delta r \\ \Delta\phi \end{bmatrix} + \begin{bmatrix} 0 & \frac{\bar{q}S}{mv_0}C_{Y_{\delta_r}} \\ \frac{\bar{q}Sb}{I_x}C_{l_{\delta_a}} & \frac{\bar{q}Sb}{I_x}C_{l_{\delta_r}} \\ \frac{\bar{q}Sb}{I_z}C_{n_{\delta_a}} & \frac{\bar{q}Sb}{I_z}C_{n_{\delta_r}} \\ 0 & 0 \end{bmatrix} \begin{bmatrix} \Delta\delta_a \\ \Delta\delta_r \end{bmatrix} + \begin{bmatrix} \dot{\beta}_{bias} \\ \dot{p}_{bias} \\ \dot{r}_{bias} \\ 0 \end{bmatrix} \tag{4.6}$$

$$\begin{bmatrix} \Delta\dot{\alpha} \\ \Delta\dot{q} \end{bmatrix} = \begin{bmatrix} -\frac{\bar{q}S}{mv_0}C_{L_\alpha} & 1-\frac{\bar{q}S\bar{c}}{2mv_0^2}C_{L_q} \\ \frac{\bar{q}S\bar{c}}{I_y}C_{m_\alpha} & \frac{\bar{q}S\bar{c}^2}{2I_yv_0}C_{m_q} \end{bmatrix} \begin{bmatrix} \Delta\alpha \\ \Delta q \end{bmatrix} + \begin{bmatrix} -\frac{\bar{q}S}{mv_0}C_{L_{\delta_e}} \\ \frac{\bar{q}S\bar{c}}{I_y}C_{m_{\delta_e}} \end{bmatrix} \begin{bmatrix} \Delta\delta_e \end{bmatrix} + \begin{bmatrix} \dot{\alpha}_{bias} \\ \dot{q}_{bias} \end{bmatrix} \tag{4.7}$$

The stability and control derivative coefficients were used instead of the dimensional stability and control derivatives since the dimensional components change quadratically with airspeed from the dynamic pressure equation; however, the dimensionless coefficients are not as intuitive and will briefly be explained. C_{m_α} is an example of a common stability derivative coefficient which is equal to the derivative of the pitching moment coefficient, shown previously in Eq. (4.2), versus angle of attack (Figure 23). When an aircraft has an angle of attack beyond the equilibrium/trim point, a negative pitch moment is produced resulting in a negative restoring moment coefficient, C_m. When the angle of attack is less than stability condition's angle of attack, C_m will be positive resulting

in the aircraft returning to its trim condition [44]. Moment coefficient derivatives with respect to control surface deflection, also described as control effectiveness coefficients, follow a similar concept (dimensional $L_{\delta a}$ is described as aileron-to-roll control effectiveness) [45]. For example, the derivation of the roll moment coefficient, C_l, versus aileron deflection, δa, results in a positive $C_{l_{\delta a}}$ (Figure 24). When both ailerons work normally, both ailerons provide a combined roll moment; however, if the left aileron experiences a fixed-position failure at $0°$, the right aileron will be half as effective as it only produces half of the roll moment. The resultant $C_{l_{\delta a}}$ derivation is approximately half of the nominal $C_{l_{\delta a}}$ derivation as this term is less effective at producing roll moments.

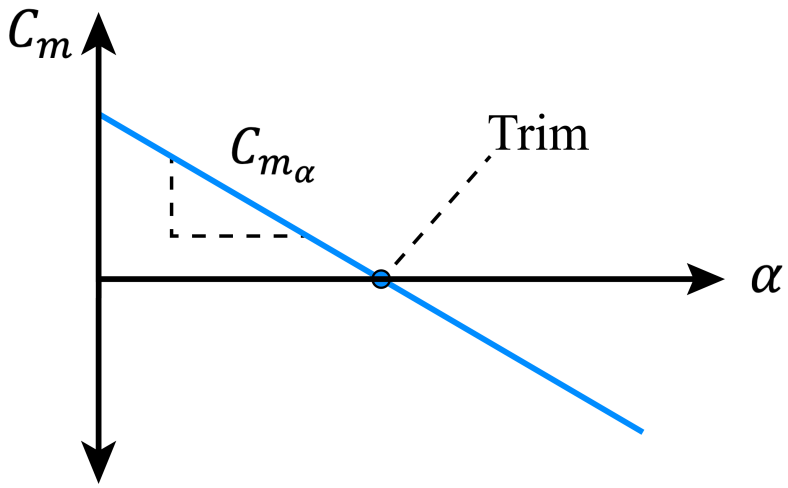

Figure 23: Pitching moment versus angle of attack.

4.3.2 Input Design

Phase-optimized orthogonal multi-sine signals were constructed using SIDPAC to excite the pitch, roll, and yaw axes of the aircraft. These input signals provide useful

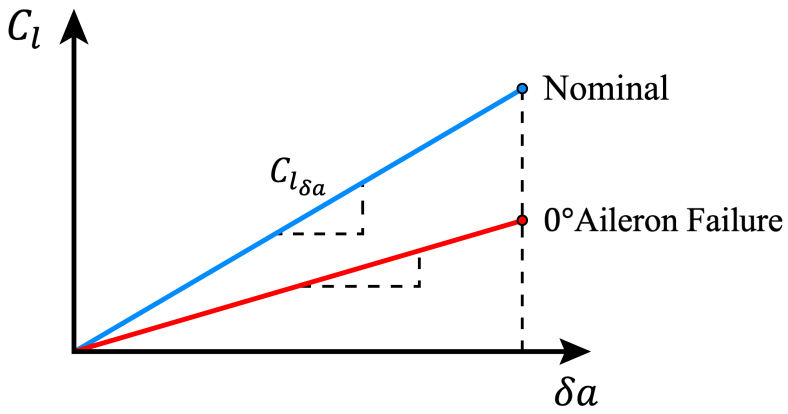

Figure 24: Roll moment versus aileron deflection.

dynamic response data and improve the modeling of the aircraft [46]. The multi-sine signal was designed such that axis collinearity was reduced, frequency-rich excitation data was provided, and minimal disturbances were induced on the aircraft during its nominal flight [47]. Collinearity is the poor conditioning of inputs where the axes components have minimal independence and the system is unexcited above the respective noise level [46]. Furthermore, each axis requires minimal collinearity to improve dynamic state estimation results while using the EKF. The multi-sine input was designed to excite a frequency range of $0.2\,\mathrm{Hz}$ to $3\,\mathrm{Hz}$ in order to capture the lower frequency content of the pitch, roll, and yaw axes of the Timber. This frequency range was considered sufficient as the dynamic modes of similar fixed-wing UAVs have be captured within a similar range [48]. The orthogonal multi-sine design used every third alternating frequency with a $0.1\,\mathrm{Hz}$ increment for the roll, pitch, and yaw axes of rotation to provide enough frequency content over the $3\,\mathrm{Hz}$ band. The roll multi-sine input signal started at $0.2\,\mathrm{Hz}$, pitch started at $0.3\,\mathrm{Hz}$, and the yaw input signal started at $0.4\,\mathrm{Hz}$.

The multi-sine input design used Eq. (4.8) where the input amplitude was configured such that the peak amplitudes were within a desired range; thus, peak factor was minimized while still maintaining a high level of axes excitation [47]. T represents the time length of excitation and k is the k_{th} frequency component of the signal. Sinusoidal phase angles were optimized using Eq. (4.9), where M represents the harmonically-related frequencies in the signal [46]. An initial amplitude of 1 was used for the Timber to provide easily scalable multi-sine signals (Figure 25). The roll axis amplitude was set to 0.2 and eventually 0.15 whereas the pitch and yaw axes were both set to 0.2 due to having less control surface area resulting in reduced moments. Table 6 and Table 7 provides the frequency and phase angle content of the multi-sine input signals.

$$u(i) = \sum_{k=1}^{M} A_k \sin\left(\frac{2\pi k t(i)}{T} + \phi_k\right) \tag{4.8}$$

$$\phi_k = \phi_{k-1} - \frac{\pi k^2}{M} \tag{4.9}$$

PX4's fixed-wing attitude module was modified to include the multi-sine input. This module combined the multi-sine signals and pilot commands which were sent to the output mixer. The mixer converts the combined signals to PWM for each of the aircraft's control surface actuators. The combined signals sent to the mixer are between -1 and 1, which correspond to a minimum and maximum PWM of $1000\ \mu$s to $2000\ \mu$s, respectively. QGroundControl was used to interface and modify the onboard multi-sine input parameters. A custom software parameter, *MSI_EN*, was used to enable and disable the multi-sine

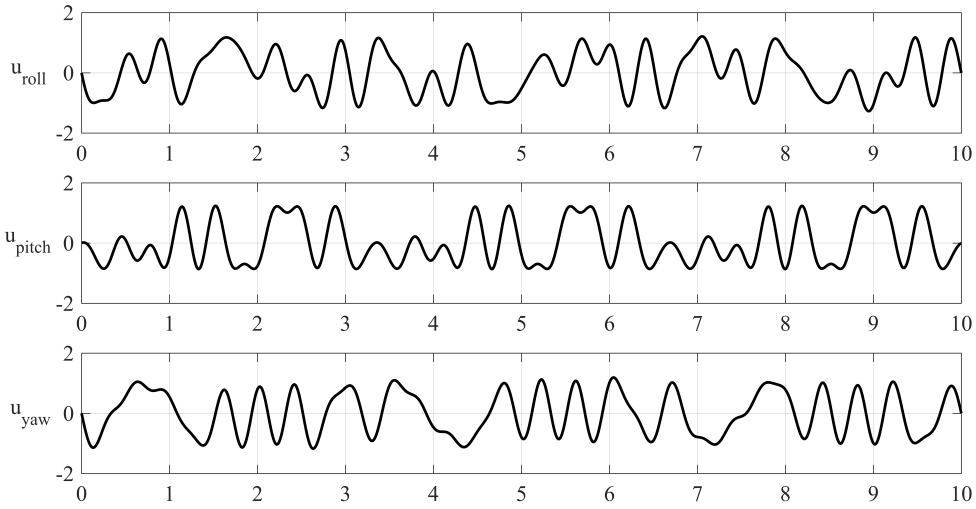

Figure 25: Multi-sine input excitation for the roll, pitch, and yaw axes.

Table 6: Frequency content in the multi-sine input signals.

Frequency Content (Hz), u_{roll}	**Frequency Content (Hz),** u_{pitch}	**Frequency Content (Hz),** u_{yaw}
0.2	0.3	0.4
0.5	0.6	0.7
0.8	0.9	1
1.1	1.2	1.3
1.4	1.5	1.6
1.7	1.8	1.9
2	2.1	2.2
2.3	2.4	2.5
2.6	2.7	2.8
2.9	3	0

Table 7: Frequency content in the multi-sine input signals.

Phase Angles (rad), u_{roll}	**Phase Angles (rad), u_{pitch}**	**Phase Angles (rad), u_{yaw}**
-2.1086	2.0781	-1.7056
1.2626	2.7096	-3.0017
2.8477	-1.0536	1.2820
1.4980	1.8934	0.4246
-0.6160	-2.6380	1.6524
1.2010	-0.3013	1.2917
0.8767	-1.0706	-2.9561
0.1924	0.8460	-0.1085
2.5206	-0.1021	1.8517
2.6782	-3.1216	0

input. Similarly, the *MSI_ROLL_AMP*, *MSI_PITCH_AMP*, and *MSI_YAW_AMP* parameters were changed to modify the multi-sine input amplitudes. The ground station was used to modify the multi-sine parameters in real-time during the testing.

4.3.3 Estimation

The EKF [2] was used, due to its expansion of the former Kalman filter (KF), to estimate both parameter coefficients and states from the aircraft's equations of motion. Traditional KFs only estimate aircraft states without estimating coefficients. If coefficients were to be estimated, the coefficients would need to be augmented to the state vector. This form of estimation leads to an expansion from the linear state estimation region to the nonlinear region (which requires an EKF) [20]. EKFs have also been used in the past and have shown to be accurate when estimating fixed-wing equations of motion with respective aerodynamic coefficients ([18–20]). Thus, the EKF was ideal for identifying failure effects on the aircraft's dynamics.

Estimation using the EKF necessitates the use of five main equations which may be divided into prediction and correction phases [17]. However, before the EKF algorithm is used for the duration of the flight test data, states and essential covariance matrices require initialization. Initial values for state estimates x_i, state measurement matrix G, process noise covariance Q, measurement noise covariance R, and error covariance matrix P are considered (Q, R, and P initial estimates are in the Appendix). Thereafter, the propagation phase updates the state estimates and error covariance matrix using the last known values from the previous time step (indicated by a superscript minus). The correction phase takes into account the propagated estimates and error covariance matrix while utilizing the Kalman gain to provide a more accurate estimate. This process is repeated until the flight concludes or until estimation is no longer required.

Figure 26 shows the EKF cycle along with the equations that are used at each step. The propagation phase predicts the next estimates as indicated by $k+1$ for both the state estimate and error covariance (Eqs. (4.10) and (4.11)). As previously mentioned, the superscript minus is indicative of an uncorrected value without any measurement information at that specific time step. F_k, often denoted as ϕ_k but changed to avoid confusion with the multi-sine phase shift notation, represents the state transition matrix which includes partial derivatives of the linearized equations with respect to the EKF state vector, x_k (important state transition equations are presented in the Appendix). The process noise covariance matrix, Q, is an $(n \times n)$ matrix where n indicates the number of states estimates. The Q matrix tuning was based on an iterative approach which concluded when the state estimates converged.

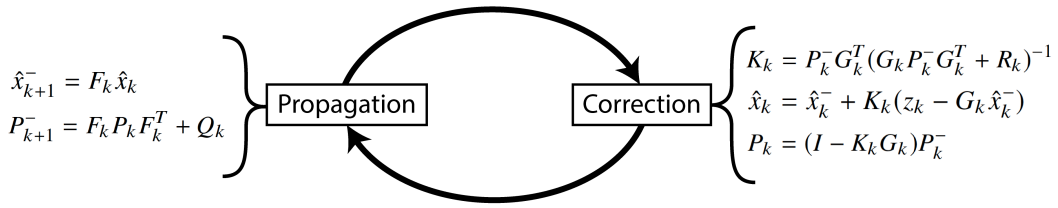

Figure 26: EKF propagation and correction phases.

$$\hat{x}_{k+1}^- = F_k \hat{x}_k \tag{4.10}$$

$$P_{k+1}^- = F_k P_k F_k^T + Q_k \tag{4.11}$$

The correction step is important as the initial propagated values may be inaccurate and exclude updated sensor measurements. The first equation used in this step is known as the Kalman gain equation (Eq. (4.12)). The Kalman gain equation reduces mean-square estimation error by incorporating the measurement noise matrix, R, and sensor measurement matrix, G ([2]). The R matrix values, described in Table 10 within the Appendix, are determined through steady-state sensor measurements where the value of R is indicative of two standard deviation bounds [19]. The sensor measurement values were determined from nominal free-flight test data and reduced by approximately half to account for any atmospheric conditions that added noise to the system. Lateral measurement values were reduced further to improve the state estimates. The G matrix is used to indicate which states have respective sensor measurements, where a value of 1 aligns with the measured state. The measurement/observation vector, z_k, is used in the estimate correction equation (Eq. (4.13)). Error covariance is then computed for the latest estimates

using Eq. (4.14) where I is the identity matrix of size $(n \times n)$ [2]. The error covariance matrix initialization used initial variance measurements of the states and was assumed to be small for the other estimation parameters (stability coefficients, control coefficients, and biases) [19]. The measurement vector, z_k included measurement data from all axes of the gyroscope, sideslip estimates from PX4, angle of attack from the wind vane sensor, and Euler angle measurements for roll. All of the sensor measurements, except angle of attack, were located at the center of gravity; thus, the angle of attack needed correction as it was extended about $0.2794\,\mathrm{m}$ along the X-axis and $-0.7493\,\mathrm{m}$ along the Y-axis. The correction, Eq. (4.15), uses roll rate, p, and pitch rate, q, along with the estimated velocity [49].

$$K_k = P_k^- G_k^T (G_k P_k^- G_k^T + R_k)^{-1} \tag{4.12}$$

$$\hat{x}_k = \hat{x}_k^- + K_k(z_k - G_k \hat{x}_k^-) \tag{4.13}$$

$$P_k = (I - K_k G_k) P_k^- \tag{4.14}$$

$$\alpha = \alpha_{measure} + \frac{q x_a - p y_a}{v} \tag{4.15}$$

Initial Timber stability coefficients were estimated using AVL for steady-level flight Table 8. The values provide an approximation of where the dimensionless coefficient estimates may converge during nominal flight. $C_{l_{\delta a}}$ was initialized as 0.05 as this

value was around the convergence value for this control coefficient. The value for $C_{l_{\delta a}}$ was also tested as 0 with no noticeable impact on the EKF estimates. All other EKF states, except for the AVL estimates, were initialized as 0.

Table 8: Stability coefficient estimates from Athena Vortex Lattice (steady-level flight).

Lateral-Directional Stability Coefficients	**Value**
C_{Y_β}	-0.183560
C_{Y_p}	0.083760
C_{Y_r}	0.154848
C_{l_β}	-0.037887
C_{l_p}	-0.491165
C_{l_r}	0.084577
C_{n_β}	0.071563
C_{n_p}	-0.027989
C_{n_r}	-0.062579

Longitudinal Stability Coefficients	**Value**
C_{L_α}	5.030962
C_{L_q}	8.626024
C_{m_α}	-1.041654
C_{m_q}	-12.567985

4.4 Results and Discussion

4.4.1 Nominal Flight Estimation

The Timber was flown manually in an ellipsoid racetrack such that the flight trajectory could deviate due to manual input and atmospheric conditions. Flight data was post-processed in an EKF to determine coefficient convergence and state estimates. The EKF estimates during nominal flight resulted in state estimates which followed the sensor measurement data, from z_k, but with less noise (Figure 27). Sideslip estimates do not follow the sideslip measurements. This is reasonable as the Timber's multi-sine yaw input was smooth which is not characteristic of the sharp rising and falling edges of the sideslip measurements. Comparatively to all of the other measured states, pitch rate was

the noisiest. This noise was accounted for in the EKF noise covariance matrix in order to estimate a more accurate pitch rate. Noise from the other measurements was accounted for as well but was not equal to that of the pitch rate noise.

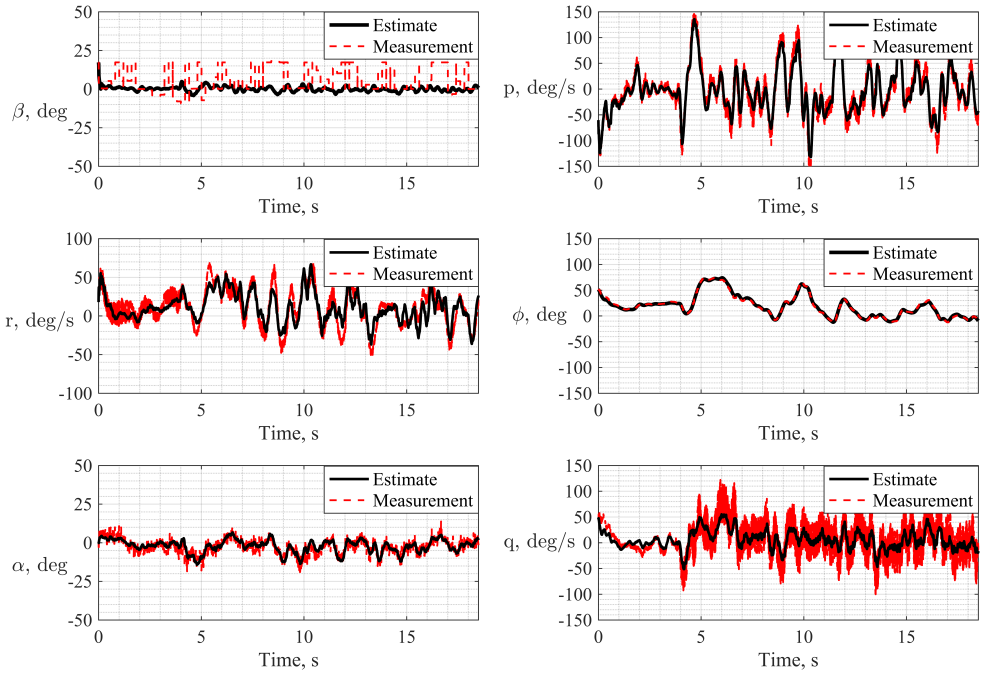

Figure 27: Time history of EKF state estimates during nominal flight.

Similarly, if initialization of the EKF states is wrong, estimates may diverge and provide poor modeling for the system. However, initial estimates from AVL were used and all lateral-directional and longitudinal coefficients showed convergence after approximately $18.5\,\mathrm{s}$ (Figure 28 and Figure 29). The convergence of EKF states provides more confidence in using the model to detect when irregularity/failures occur. It is important to note that C_{m_α} and C_{n_β} converged to values that were different than the initial estimates.

Although this is not ideal, there are many factors that could have caused this behavior. In typical dynamic modeling and fixed-wing research, an aircraft is outfitted with a differential pressure sensor, which uses pitot static tube, in order to provide accurate airspeed measurements [50]; however, the Timber testing did not use a differential pressure sensor and pitot static tube but instead relied on the magnitude of the body-fixed velocity estimates (PX4 estimates velocity along the X-axis, Y-axis, and Z-axis). The Timber's velocity during a nominal flight varied between $19.5\,\mathrm{m/s}$ and $10.8\,\mathrm{m/s}$ at a frequency of $10\,\mathrm{Hz}$ whereas the GPS velocity estimates varied between $24\,\mathrm{m/s}$ and $10.2\,\mathrm{m/s}$ at a frequency of about $5\,\mathrm{Hz}$ (Figure 30). The onboard Timber velocity estimate was used in the EKF as it provided a higher measurement frequency than the GPS estimate. Since the aircraft's airspeed varied throughout the testing, it is reasonable that added noise would reduce the accuracy of the stability coefficient estimates. However, for the purpose of this testing, convergence was important regardless of the change from the initial estimates. If the nominal flight data resulted in estimate divergence, then the EKF would be poorly conditioned resulting in less accurate modeling. Since the EKF's state estimates took approximately $18.5\,\mathrm{s}$ to converge, nominal flight time was around $20\,\mathrm{s}$ to $30\,\mathrm{s}$ before any failure occurred. To further provide confidence in the EKF, coefficients such as C_{l_p}, C_{n_r}, and C_{m_q} were assessed to ensure the EKF model was designed appropriately for the Timber. These terms were expected to be negative as these coefficients are damping terms for the aircraft. All of the damping coefficients converged to values less than zero as expected, which provided more confidence in using the EKF (Figure 28 and Figure 29).

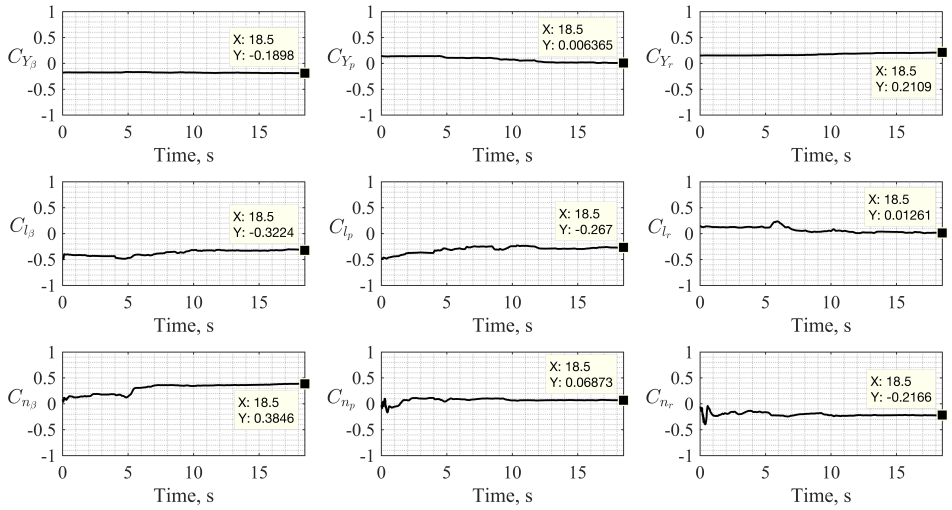

Figure 28: Aircraft lateral-directional stability coefficient estimates during nominal flight.

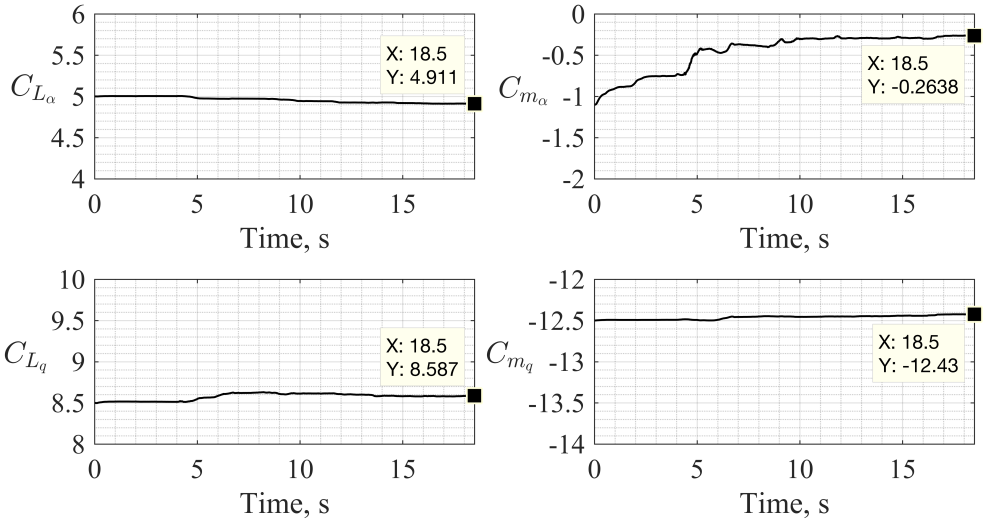

Figure 29: Aircraft longitudinal stability coefficient estimates during nominal flight.

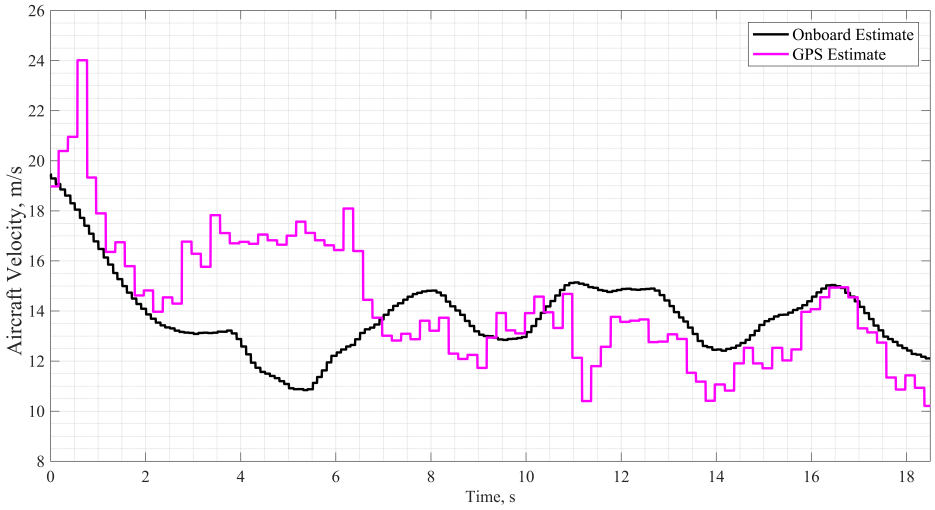

Figure 30: Aircraft velocity measurements during nominal flight with active multi-sine input.

4.4.2 Fixed-Position Aileron Failures

Each fixed-position aileron test started with approximately $20\,\mathrm{s}$ to $30\,\mathrm{s}$ of nominal flight. The first fixed-position failure that was tested was a neutral $0°$ failure. Thereafter, tests varied the fixed-position deflection angle by $10°$ within the range of $30°$ to $-30°$. Once the failure occurred, the pilot maneuvered the aircraft for another $20\,\mathrm{s}$ to $30\,\mathrm{s}$ or until the aircraft was rendered uncontrollable. The pilot was able to control the $0°$, $-10°$, and $10°$ fixed-position failures, but deflection angles beyond those failures resulted in uncontrollable flight (pilot was unable to follow the ellipsoid flight pattern due to trajectory deviations). During balanced fixed-position failures (net roll moment equal to 0), both ailerons act similarly to an elevator, creating a pitching moment. Although the pilot was able to quickly adjust for the new flight condition, an autopilot may be able to better correct for all of the adverse moments produced by the failure.

Figure 31 shows the EKF estimates for $C_{L_{\delta a}}$. Each test was aligned to show $10\,\mathrm{s}$ before the failure and $15\,\mathrm{s}$ after the failure. The vertical red line indicates when the failure occurred (this red line is used in all other failure figures to indicate when a failure occurred). As mentioned in Section 4.3.1, the change in the aileron effectiveness coefficient is expected to reduce as only half of the aileron control surfaces work nominally. All of the fixed-position tests except the 10° test resulted in a $C_{L_{\delta a}}$ estimate reduction within $2\,\mathrm{s}$ whereas the 10° test took approximately $12\,\mathrm{s}$ to reduce its aileron effectiveness coefficient (Table 9). It is reasonable for fixed-position failures greater than 10° and less than -10° to indicate immediate dynamic changes in the aileron's coefficient estimate as the aircraft's flight maneuver suddenly changes due to a fixed-position failure. Thus, a fixed-position deflection angle that is closer to 0° results in more control and less of an adverse roll moment. Figure 31 also shows failure tests that end a few seconds after the failure occurred indicating that the pilot disabled the failure to avoid crashing the aircraft (left aileron returned to nominal control). The 0° and $\pm 10^\circ$ failures were controllable by a pilot in manual mode for upwards of $30\,\mathrm{s}$. The final estimates for all of the fixed-position failures resulted in a $C_{L_{\delta a}}$ reduction. The $\pm 30^\circ$ fixed-position failures resulted in a $C_{l_{\delta a}}$ reduction close to $50\,\%$ which is expected as the control effectiveness is reduced by $50\,\%$ from the failure (based on the time of failure estimate and last estimate shown in Table 9). The 0° test resulted in a $C_{L_{\delta a}}$ percentage change of $44.89\,\%$ and $74.47\,\%$ for $2\,\mathrm{s}$ after the failure and for the last estimate, respectively. Similarly, each respective failure angle, positive and negative, resulted in a similar reduction to the $C_{l_{\delta a}}$ coefficient where the percentage change for most of the failures was

greater than $50\,\%$.

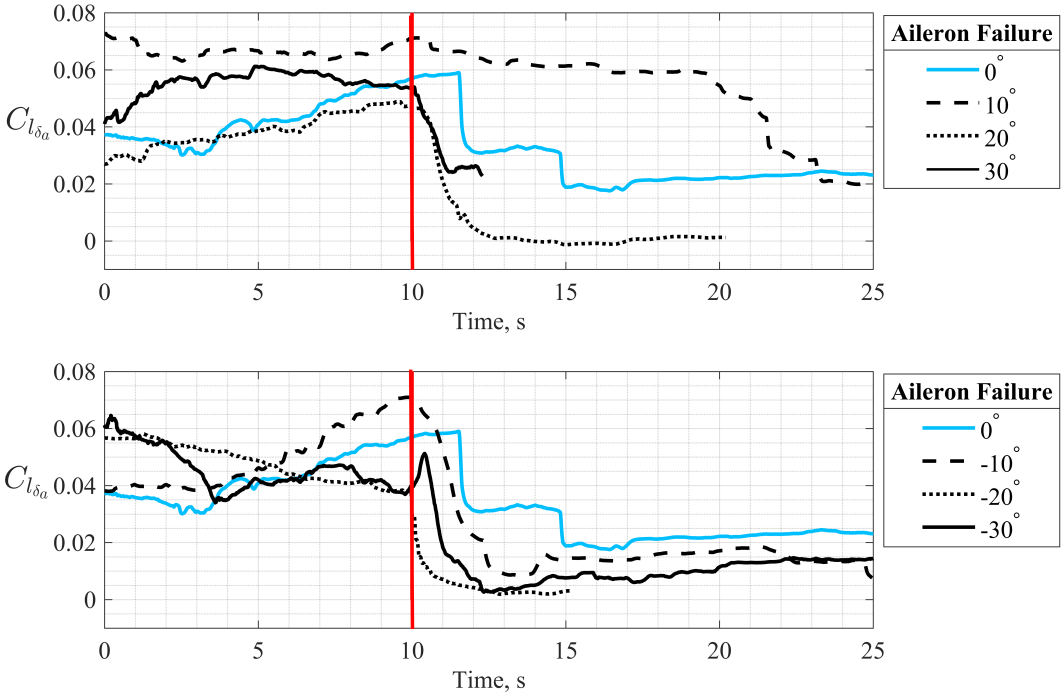

Figure 31: EKF state estimates for the roll moment coefficient with respect to aileron deflection.

It is important to note that other lateral-directional control coefficients were affected as a result of the left aileron's fixed-position failure (Figure 32). This result is reasonable as the aircraft's flight behavior changes after the failure occurs. Such changes in the control effectiveness coefficients could produce false failure identification on the other control surfaces; however, the roll moment control coefficients experienced the largest changes within $2\,\mathrm{s}$ after the failure occurred (specifically $C_{l_{\delta r}}$). $C_{n_{\delta r}}$ also experienced a large change to its estimate but only after about $4\,\mathrm{s}$. $C_{n_{\delta r}}$ also experienced more noise than the other estimates which should be considered when identifying the specific control

Table 9: $C_{L_{\delta a}}$ estimates at time of failure, 2 s after, last available estimate, and percentage change from time of failure to the last estimate.

Fixed-Position Failure	**$C_{L_{\delta a}}$ Estimate at Time of Failure (10 s)**	**$C_{L_{\delta a}}$ Estimate at 12 s**	**$C_{L_{\delta a}}$ Last Estimate**	**Percent Change**
$+30°$	0.0536	0.0258	0.0228	57.54
$+20°$	0.0470	0.0047	0.0012	97.45
$+10°$	0.0711	0.0646	0.0161	77.36
$0°$	0.0568	0.0313	0.0145	74.47
$-10°$	0.0710	0.0224	0.0176	75.21
$-20°$	0.0308	0.0042	0.0031	98.99
$-30°$	0.0397	0.0073	0.0203	48.87

surface failure as noise may trigger false failure identification.

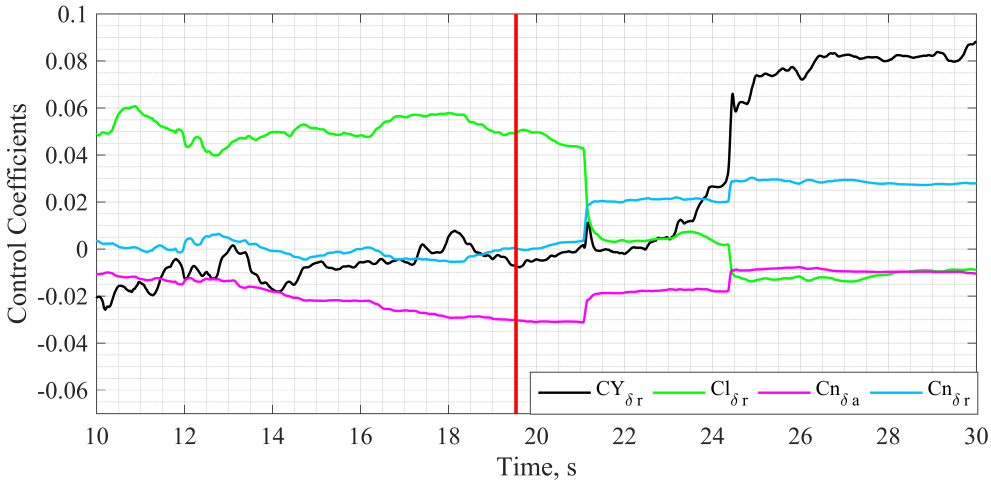

Figure 32: Other affected control coefficients during the $0°$ aileron failure.

Fixed-position failures were moderately controllable by the pilot. The pilot was able to fly the ellipsoid racetrack trajectory during the $0°$ and $\pm 10°$ fixed-position aileron failures. More severe failures, such as the $30°$ fixed-position failure, were uncontrollable within seconds of the failure occurring. This result indicates that the failure should be identified within $2\,\mathrm{s}$ for more severe fixed-position failures in order to mitigate the failure.

Less severe fixed-position failures do not require immediate identification as the adverse moments are not as severe; however, the faster the failure is identified, the faster the adaptive flight controller can adjust to mitigate the failure.

4.4.3 Aerial Delivery Failures

4.4.3.1 Center of Gravity Payload Failure

The first payload drop scenario was the CG drop where the payload released from the CG bay and the parachute remained attached inside the bay. The payload was able to swing freely under the aircraft by its riser line. The pilot was able to fly the aircraft in its failed CG state with minor flight path irregularities for about $20\,\mathrm{s}$. Similarly, the aircraft experienced minimal visible performance deviations during the flight indicating that the EKF may have some difficulties with estimating this failure. Figure 33 shows the lateral stability coefficients which remain largely unaffected (vertical red line indicates when the failure occurred). The Y force stability coefficients experienced estimation drift and never completely converged except around $50\,\mathrm{s}$ (excluding C_{Y_β}). This result was unexpected as the aircraft flew for upwards of $40\,\mathrm{s}$.

The roll rate state estimate and roll rate measurement show a change in the noise levels post-failure (Figure 34). Before the failure, the measurement noise was nominal; however, the sensor's noise reduced after the failure occurred which could be from a change in the mass properties of the aircraft (i.e. the payload increased the moment of inertia when released). It is important to note that the expected noise in the EKF's measurement noise covariance matrix does not change which may affect other state estimates.

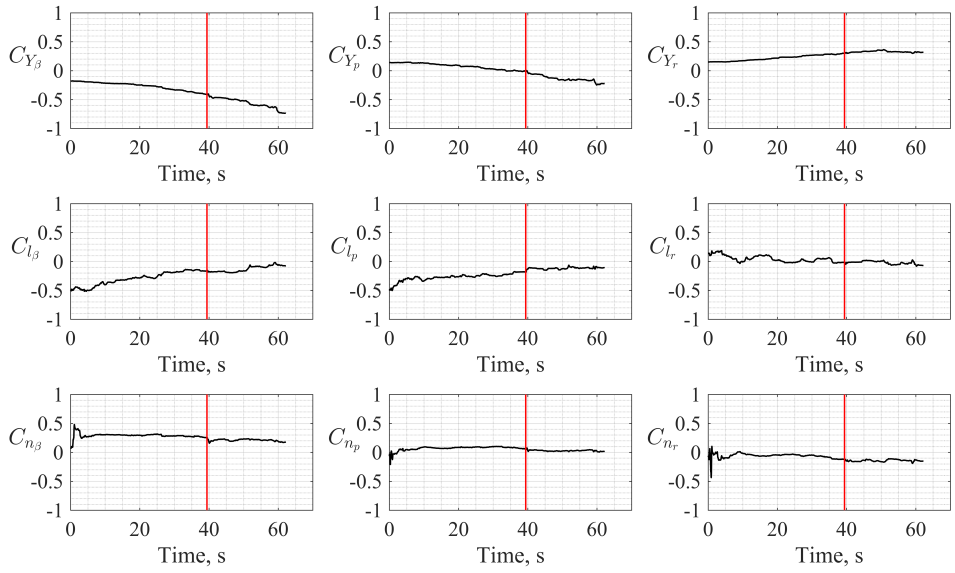

Figure 33: Lateral-directional stability coefficient estimates for the center of gravity payload failure.

The CG payload failure also resulted in control coefficient changes (Figure 35). Similar to the fixed-position aileron failures, the control coefficients changed after the failure occurred. There is an instant where the coefficients deviate before the failure occurred around $36\,\mathrm{s}$, but may be due to other flight performance factors. In order to confirm that a change in the estimates was due to a failure, other measurements and estimates should be considered. The roll rate noise is one estimate, which was previously mentioned, that may be used to ensure a failure actually did occur. Similarly, the accelerometer data may be analyzed to detect a large force and respective acceleration on the aircraft's axes from the payload weight dropping. X-axis and Z-axis accelerometer data indicate the moment the payload fully extended from the CG position (circled in red in Figure 36). There is about a $0.4\,\mathrm{s}$ delay from when the payload was initially released to when the payload reached

its maximum tangled position, $0.4318\,\mathrm{m}$ away from the CG. Although the accelerometer data is noisy due to propeller vibration, the accelerometer may be used in the future for detecting similar payload failures which induce large accelerations.

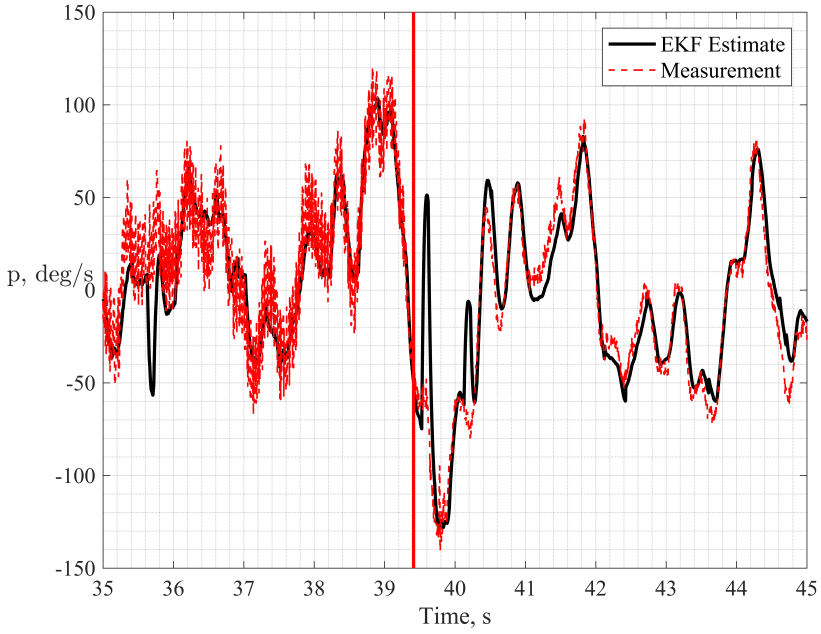

Figure 34: Roll rate estimate and sensor measurement data during the center of gravity payload failure.

When considering CG-based payload drops, careful design of the release mechanism may mitigate any payload related failure. This failure resulted in controllable flight but was considered catastrophic for fixed-wing landing; UAVs with vertical take-off and landing capabilities may be able to mitigate this type of failure through controlled descent. Furthermore, the data from this failure indicates the system's mass properties changed which may have resulted in less noise along the roll axis.

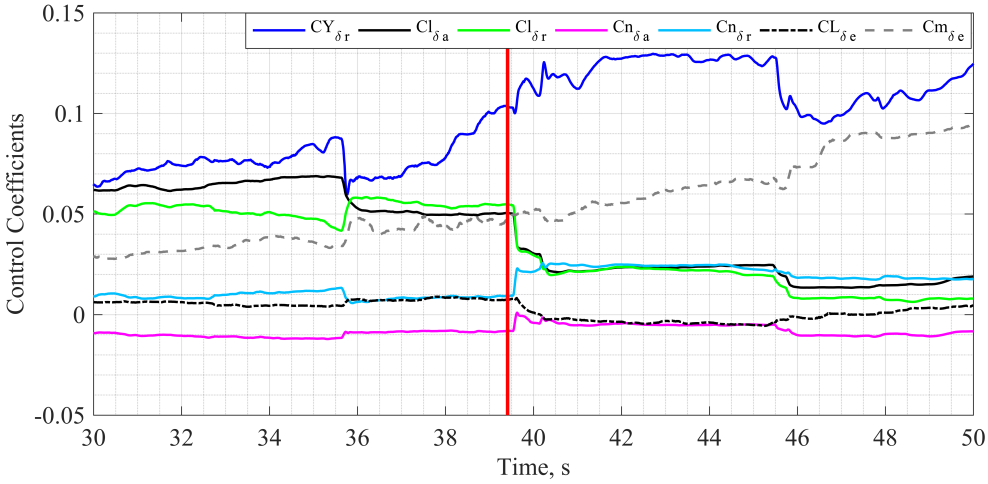

Figure 35: Lateral-directional and longitudinal control coefficient estimates during the center of gravity payload failure.

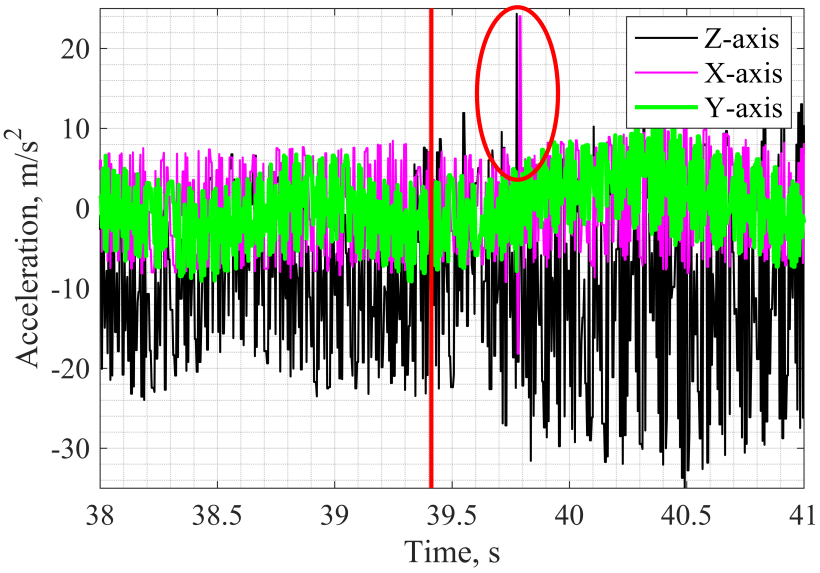

Figure 36: Unfiltered accelerometer data during the center of gravity payload failure (red circle indicates when the payload was fully released).

4.4.3.2 Wing Bay Payload Failure

The second payload drop scenario was the wing bay parachute release failure. In this scenario, payloads were attached on both wing bays and released at the same time using electromagnets. The payload and parachute on the right wing released successfully; however, the payload on the left wing bay did not release whereas its parachute did release. The increased drag on the left side of the aircraft resulted in initial negative yaw and negative pitching moments. Figure 37 shows the wing bay payload failure and its corresponding effect on the aircraft leading to a rolling nosedive trajectory (negative roll moment). This scenario was more catastrophic than the CG payload release scenario as the aircraft was rendered uncontrollable seconds after the parachute was released.

Figure 37: Timber UAV nosedive trajectory during the wing bay payload failure.

The EKF's angle of attack state estimate resulted in large deviations which was

caused by the instrumentation (Figure 38). For instance, the angle of attack sensor's measurement and estimate dropped to approximately -90° for half a second from the initial nosedive, which is indicative of a negative angle of attack; however, the -90° measurement is incorrect due to sensor saturation (angle of attack cannot accurately measure beyond a 180° range or 90° to -90°). It is important to note that the angle of attack wind vane sensor is sensitive to high velocity maneuvers. This sensitivity causes the wind vane to rotate to align with the rolling nosedive velocity vector. The saturated angle of attack measurements resulted in longitudinal coefficient estimate deviations seconds after the failure occurred. Furthermore, the lateral-directional and longitudinal stability coefficient estimates indicate that the UAV's dynamics have changed. This estimation model was poorly conditioned for this type of failure since small perturbation theory was violated (Figure 39 and Figure 40). This exact failure may be difficult to identify since every estimate experiences some form of deviation or divergent behavior. This failure also indicates that a different model may be used to better improve estimation. However, time of failure is identifiable after about $2\,\mathrm{s}$ as that is how long it took for most of the lateral-directional and longitudinal force and moment derivative coefficients to change. Certain terms such as C_{l_p} and C_{n_p} changed within about $1\,\mathrm{s}$ which is reasonable as the payload is mounted on the aircraft's wing.

The wing bay payload failure was catastrophic for a fixed-wing UAV. This outcome indicates that a similar catastrophic effect may occur with VTOL UAVs. Wing bay

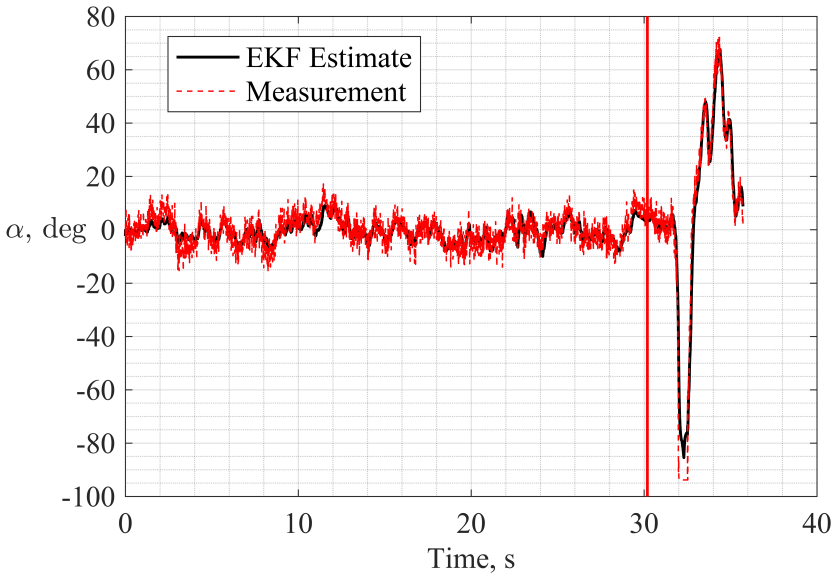

Figure 38: Angle of attack estimate and measurement during the wing bay payload scenario.

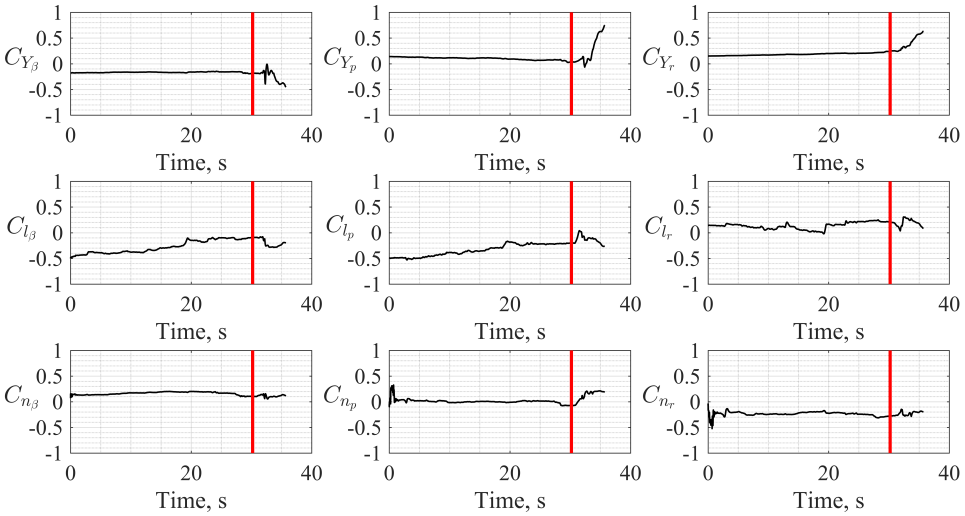

Figure 39: Lateral-directional stability coefficient estimates for the left wing bay parachute release with a stuck payload.

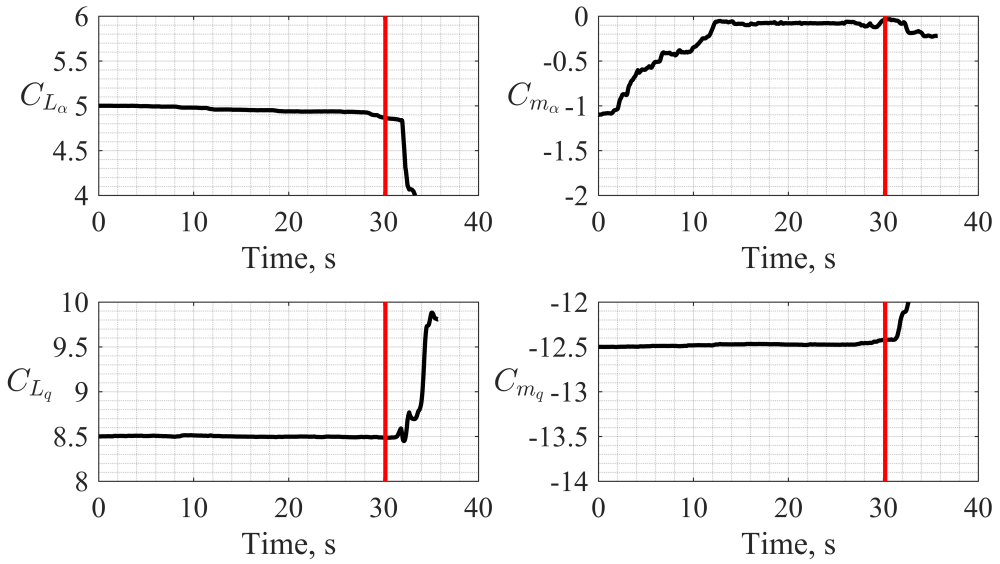

Figure 40: Longitudinal stability coefficient estimates for the left wing bay parachute release with a stuck payload.

failures should be carefully designed similar to CG payload drops such that the mechanism does not cause a release failure. Furthermore, mass property changes may potentially trigger false failure identification during nominal flight as a majority of the take-off weight is suddenly released.

4.5 Conclusion

As more UAVs are developed to fly in urban environments, safety becomes a primary concern. Failure scenarios should be considered and UAVs should be designed to mitigate any foreseeable problems that may arise. This study focused on implementing an EKF and assessing system identification models during UAV control surface failures and payload failures without instrumenting the aircraft with a differential pressure sensor

and pitot static tube. The left aileron of the E-Flite Turbo Timber experienced fixed-position failures while flying in an ellipsoid racetrack trajectory. Fixed-position failures ranged from -30° to 30° with 10° increments. The aileron's control effectiveness coefficient, $C_{l_{\delta a}}$, reduced by about $50\,\%$ or more during all of the fixed-position failure tests which was expected. This result indicates that an EKF may be used to identify fixed-position aileron failures but should be carefully designed to account for smaller changes from other control coefficient terms so as not to identify a false failure.

The payload drop failure scenarios were twofold, a center of gravity release and a wing bay release. The center of gravity release resulted in controllable flight, minor control effectiveness coefficient changes, and measurement noise changes. This failure was not catastrophic for free-flight but may result in disastrous landing maneuvers for fixed-wing UAVs; however, VTOL aircraft may be able to land safely during this failure. Identification of this failure is more difficult than aileron failure identification and may be mitigated through proper design of the payload release mechanism. The second payload scenario was the wing bay payload failure where a payload and parachute on the right side released correctly while a payload and parachute on the left side did not release correctly. The payload on the left side remained attached whereas its parachute was released, adding a large drag force to the left side of the aircraft. This failure scenario was disastrous for the fixed-wing UAV as the aircraft entered a nosedive rolling descent regardless of piloted inputs. Therefore, this scenario was considered unrecoverable for both VTOL and fixed-wing UAVs. Furthermore, the nosedive descent caused every stability and control derivative coefficient to change. This failure may be mitigated similarly to the CG payload

failure or by never using wing-based payload releases. False failure detection should be considered when using system identification for this scenario as nominal wing bay payload drops result in large mass property changes for smaller UAVs.

This research expands on the assessment of system identification models during control surface and payload failures using an EKF. Lateral-directional and longitudinal stability and control coefficient terms and aircraft states were estimated during nominal flight and failure scenarios. Estimates for these terms converged during nominal free-flight, but were subject to drift and deviations during some of the failure scenarios. However, by further instrumenting the aircraft and using higher autonomy control, the stability and control coefficients may be estimated more accurately while simultaneously identifying different hardware failures.

CHAPTER 5

CONCLUSIONS

This work outlines the importance of implementing state estimation algorithms in simulation and real-world applications. Oftentimes, these applications require system modeling but are affected by sensor noise contamination. However, this sensor noise contamination may be mitigated through the usage of state estimation algorithms. Thus, the purpose of the research was to demonstrate the utility of Kalman Filters (KF) and Extended Kalman Filters (EKFs) through describing how these state estimation algorithms apply to different scenarios; applying a KF for linear applications and EKF for nonlinear applications. An objective of using low-cost sensors was achieved and highlighted the importance of implementing these algorithms to reduce measurement uncertainty.

The first experiment centered around the implementation of a KF to improve position estimation using a simulated tracking sensor for a pursuer-evader scenario. Miss distance was the focus for this experiment and showed that a KF improved the pursuer's miss distance during most of the engagements. The KF also expanded the modeling capabilities, providing accurate velocity estimates of the evading aircraft. Throughout the duration of the pursuer-evader engagements, uncertainty from the KF state estimates decreased and outperformed the non-KF approach. Furthermore, the position uncertainty improvement due to using a KF with a lower quality sensor (higher measurement uncertainty) was comparable to using a higher quality sensor (less measurement uncertainty).

The second experiment used an EKF and low-cost sensors to evaluate lateral-directional and longitudinal dynamics of a fixed-wing aircraft during a multitude of free-flight hardware failures. When considering aileron control surface failures, the magnitude of the expected dimensionless control derivative estimates from the EKF reduced by approximately $50\,\%$ or more; the change in the effectiveness estimate indicates the ability to detect this particular failure. Aerial delivery failures were twofold. The first delivery release failure was center of gravity based and resulted in controllable flight, minor control derivative changes, and measurement noise changes. The detection of this delivery failure may be difficult as control derivative estimates resulted in smaller magnitude changes post-failure; however the change in noise characteristics was noticeable with roll rate, which indicates the potential to detect this failure using a fault detection system that focuses on noise. The second aerial delivery failure was a wing bay payload failure which resulted in estimate changes for every stability and control derivative. This payload failure was considered unrecoverable due to the large adverse moment imposed on the aircraft. This type of delivery failure was the most catastrophic failure tested and requires a fault detection and isolation controller that reacts within seconds to counter the unwanted aircraft response.

When considering the implementation of these algorithms, special care should be taken to understand the objectives of each scenario and application. Similarly, care should be taken for the mathematical model selection as each model may constrain the state estimation algorithm that is used. This constraint was exemplified when the EKF was used instead of the KF for the second experiment to estimate the aircraft states; the KF is unable

to estimate all of the aircraft states with the same performance as the EKF. In both experiments, the modeling capabilities of each system were expanded and improved as more state variables were estimated as opposed to what was possible without implementing a KF or EKF.

5.1 Future Work

Future implementation of these state estimation algorithms should consider onboard and off-board sensor interaction. While implementing a state estimation algorithm for a pursuer-evader scenario, parameter interaction between the algorithm and the pursuer control logic should be assessed. Furthermore, an optimal proportional navigation gain may work better with different tracking measurement uncertainty and should be tested. The pursuer-evader scenario could be expanded to consider a maneuvering evader as the maneuvering evader may improve state estimation results as opposed to using only raw tracking measurements. If a maneuvering evader is considered, then the evader's process model could be changed in order to account for changes in acceleration. Implementation of an Extended Kalman Filter may be better suited for a maneuvering evader and may further improve the pursuer's miss distance results.

Free-flight hardware failures associated with other control surfaces should be evaluated. Furthermore, hardware redundancy should be assessed and more fault isolation procedures should be developed. Similarly, more aerial delivery failures should be evaluated as drone delivery becomes mainstream. Methods of mitigating large adverse moments on aircrafts should be considered and tested as these failures result in catastrophic

free-flight effects. The identification of these hardware failures within seconds is important and raises concerns for the onboard location of these payloads. Finally, further studies related to false alarms should be conducted with the development of a common fault detection architecture.

APPENDIX A

ADDITIONAL RESULTS

A.1 Experiment 2: Free-Flight Failure Scenario

Table 10: EKF initial process noise, measurement noise, and error covariance matrices.

Lateral States & Parameters	**Q**	**R**	**P**
$\dot{\beta}$	10^{-1}	-	10^{-3}
$\dot{p}$	10^{-1}	-	10^{-3}
$\dot{r}$	10^{-1}	-	10^{-3}
$\dot{\phi}$	10^{-4}	-	10^{-3}
β	10^{-5}	2.5944	2.5944
p	10^{-5}	2.4188	2.4188
r	10^{-5}	2.4985	2.4985
ϕ	10^{-5}	0.1205	0.1205
C_{Y_β}	10^{-9}	-	10^{-5}
C_{Y_p}	10^{-9}	-	10^{-5}
C_{Y_r}	10^{-9}	-	10^{-5}
$C_{Y_{\delta r}}$	10^{-12}	-	10^{-5}
C_{l_β}	10^{-10}	-	10^{-5}
C_{l_p}	10^{-10}	-	10^{-5}
C_{l_r}	10^{-10}	-	10^{-5}
$C_{l_{\delta a}}$	10^{-12}	-	10^{-3}
$C_{l_{\delta r}}$	10^{-12}	-	10^{-3}
C_{n_β}	10^{-10}	-	10^{-4}
C_{n_p}	10^{-10}	-	10^{-3}
C_{n_r}	10^{-10}	-	10^{-3}
$C_{n_{\delta a}}$	10^{-12}	-	10^{-3}
$C_{n_{\delta r}}$	10^{-12}	-	10^{-3}
$\dot{\beta}_{bias}$	10^{-4}	-	10^{-3}
$\dot{p}_{bias}$	10^{-4}	-	10^{-3}
$\dot{r}_{bias}$	10^{-4}	-	10^{-3}

Longitudinal States & Parameters	**Q**	**R**	**P**
$\dot{\alpha}$	10^{-1}	-	10^{-3}
$\dot{q}$	10^{-1}	-	10^{-3}
α	10^{-2}	1.9410	1.9410
q	10^{-2}	17.8582	17.8582
C_{L_α}	10^{-8}	-	10^{-4}
C_{L_q}	10^{-8}	-	0.008
$C_{L_{\delta e}}$	10^{-10}	-	10^{-4}
C_{m_α}	10^{-9}	-	10^{-4}
C_{m_q}	10^{-9}	-	10^{-4}
$C_{m_{\delta e}}$	10^{-10}	-	10^{-4}
$\dot{\alpha}_{bias}$	10^{-4}	-	10^{-4}
$\dot{q}_{bias}$	10^{-4}	-	10^{-4}

Table 10 provides the initialized Q, R, and P estimates for the lateral-directional and longitudinal aircraft dynamics for every failure scenario that was tested in this study. The important state transition matrix equations are shown in Eq. (A.1) to Eq. (A.12) where the aircraft's states follow kinematic equations and the respective state derivatives follow the linearized longitudinal-directional and lateral equations of motion. Table 11 indicates which X_k corresponds to each EKF state. All of the coefficients and bias terms were assumed to be constant so these states were set to equal the previous time step (i.e. $C_{L_{\delta e}}$: $X_k(32) = X_{k-1}(32)$).

$$F_1 = \frac{\rho Sv}{2m}X_k(9)X_k(5) + \frac{\rho Sb}{4m}X_k(10)X_k(6) + \frac{\rho Sb}{4m}X_k(11)X_k(7) - X_k(7) + \frac{g\cos\theta_0}{v}X_k(8) + \frac{\rho Sv}{2m}X_k(12)\delta r + Xk(13) \tag{A.1}$$

$$F_2 = \frac{\rho Sbv^2}{2I_x}X_k(14)X_k(5) + \frac{\rho Sb^2v}{4I_x}X_k(15)X_k(6) + \frac{\rho Sb^2v}{4I_x}X_k(16)X_k(7) + \frac{\rho Sbv^2}{2I_x}X_k(17)\delta a + \frac{\rho Sbv^2}{2I_x}X_k(18)\delta r + X_k(19) \tag{A.2}$$

$$F_3 = \frac{\rho Sbv^2}{2I_z}X_k(20)X_k(5) + \frac{\rho Sb^2v}{4I_z}X_k(21)X_k(6) + \frac{\rho Sb^2v}{4I_z}X_k(22)X_k(7) + \frac{\rho Sbv^2}{2I_z}X_k(23)\delta a + \frac{\rho Sbv^2}{2I_z}X_k(24)\delta r + X_k(25) \tag{A.3}$$

$$F_4 = X_k(6) \tag{A.4}$$

$$F_5 = X_k(5) + X_k(1)\Delta t \tag{A.5}$$

$$F_6 = X_k(6) + X_k(2)\Delta t \tag{A.6}$$

$$F_7 = X_k(7) + X_k(3)\Delta t \tag{A.7}$$

$$F_8 = X_k(8) + X_k(4)\Delta t \tag{A.8}$$

$$F_{26} = X_k(29) - \frac{\rho S v}{2m}(X_k(30)X_k(28) + \frac{\bar{c}}{2v}X_k(31)X_k(29) + X_k(32)\delta e) + X_k(33) \tag{A.9}$$

$$F_{27} = \frac{\rho S \bar{c} v^2}{2I_y}(X_k(34)X_k(28) + \frac{\bar{c}}{2v}X_k(35)X_k(29) + X_k(36)\delta e) + X_k(37) \tag{A.10}$$

$$F_{28} = X_k(28) + X_k(26)\Delta t \tag{A.11}$$

$$F_{29} = X_k(29) + X_k(27)\Delta t \tag{A.12}$$

Figure 41 provides the lateral-directional stability derivative coefficient estimates during the 0° fixed-position failure test. Figure 42 provides the longitudinal stability derivative coefficient estimates during the 0° fixed-position failure test.

Figure 43 shows the longitudinal stability coefficient estimates during the center of gravity failure. The estimate of the C_{m_α} converged as a positive value. Figure 44 provides the control coefficient changes during the wing bay payload release failure. $C_{y_{\delta r}}$ did not converge before the failure occurred; however, the other control coefficients did show convergence.

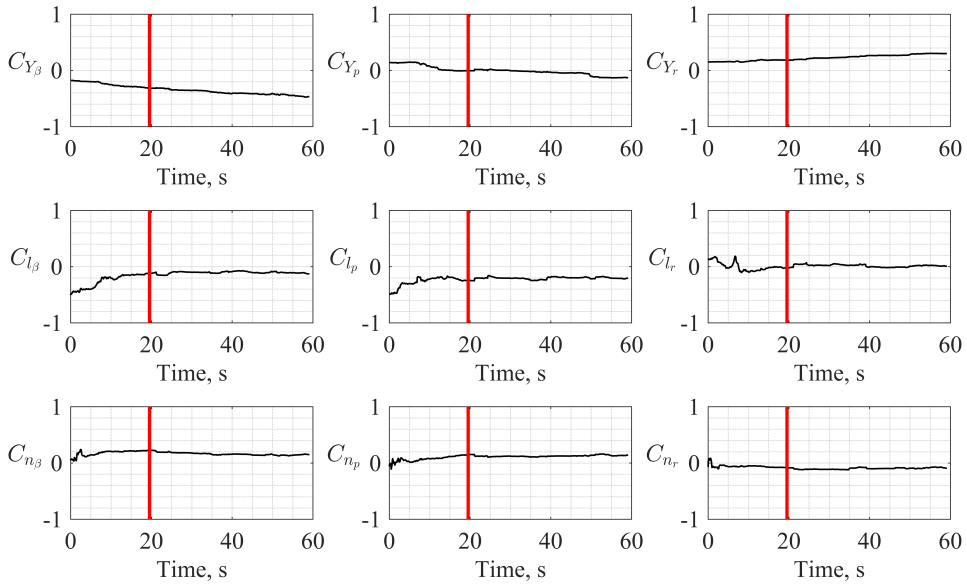

Figure 41: Lateral-directional stability derivative coefficients during the 0° fixed-position aileron failure test.

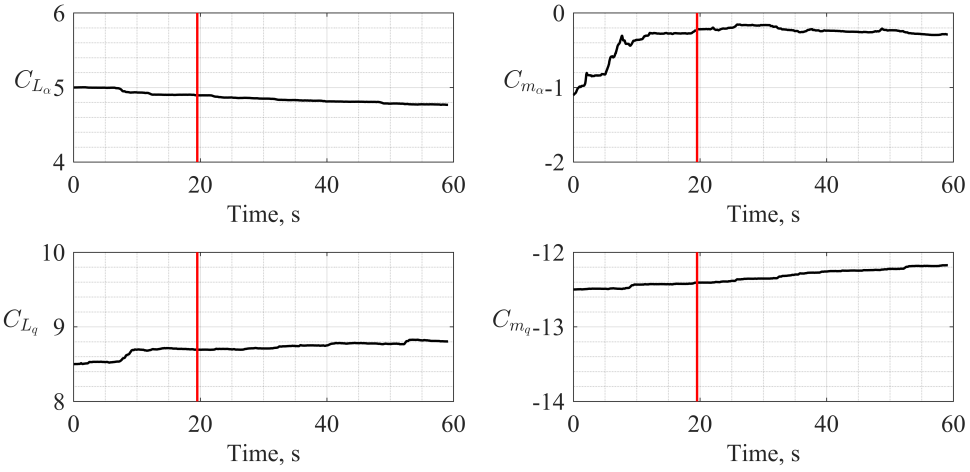

Figure 42: Longitudinal stability derivative coefficients during the 0° fixed-position aileron failure test.

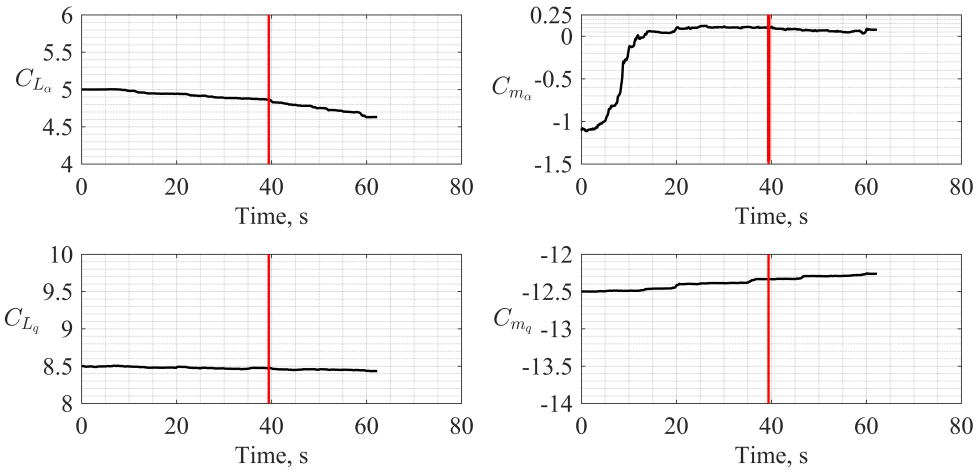

Figure 43: Longitudinal stability derivative coefficients during the center of gravity payload failure.

Table 11: EKF parameters and corresponding lateral-directional and longitudinal variables.

X_k	**Lateral-Directional States & Parameters**
$X_k(1)$	$\dot{\beta}$
$X_k(2)$	$\dot{p}$
$X_k(3)$	$\dot{r}$
$X_k(4)$	$\dot{\phi}$
$X_k(5)$	β
$X_k(6)$	p
$X_k(7)$	r
$X_k(8)$	ϕ
$X_k(9)$	C_{Y_β}
$X_k(10)$	C_{Y_p}
$X_k(11)$	C_{Y_r}
$X_k(12)$	$C_{Y_{\delta r}}$
$X_k(13)$	$\dot{\beta}_{bias}$
$X_k(14)$	C_{l_β}
$X_k(15)$	C_{l_p}
$X_k(16)$	C_{l_r}
$X_k(17)$	$C_{l_{\delta a}}$
$X_k(18)$	$C_{l_{\delta r}}$
$X_k(19)$	$\dot{p}_{bias}$
$X_k(20)$	C_{n_β}
$X_k(21)$	C_{n_p}
$X_k(22)$	C_{n_r}
$X_k(23)$	$C_{n_{\delta a}}$
$X_k(24)$	$C_{n_{\delta r}}$
$X_k(25)$	$\dot{r}_{bias}$

X_k	**Longitudinal States & Parameters**
$X_k(26)$	$\dot{\alpha}$
$X_k(27)$	$\dot{q}$
$X_k(28)$	α
$X_k(29)$	q
$X_k(30)$	C_{L_α}
$X_k(31)$	C_{L_q}
$X_k(32)$	$C_{L_{\delta e}}$
$X_k(33)$	$\dot{\alpha}_{bias}$
$X_k(34)$	C_{m_α}
$X_k(35)$	C_{m_q}
$X_k(36)$	$C_{m_{\delta e}}$
$X_k(37)$	$\dot{q}_{bias}$

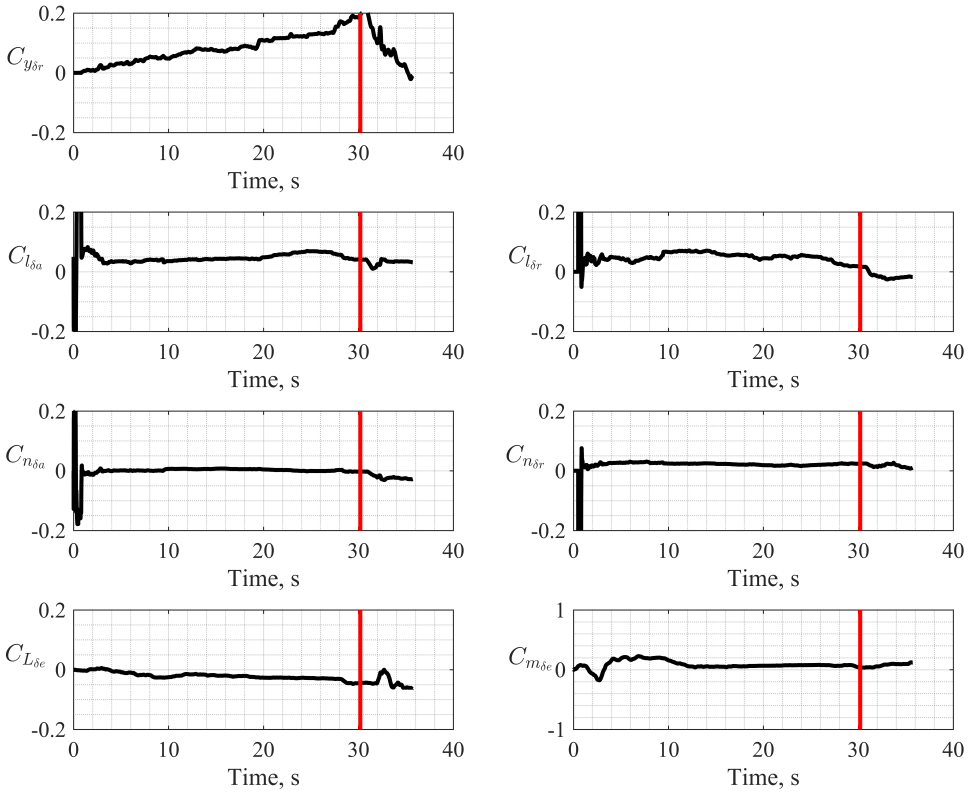

Figure 44: Control coefficient changes during the wing bay payload release failure.

REFERENCE LIST

[1] Tischler, M. B., and Remple, R. K., *Aircraft and Rotorcraft System Identification*, 2nd ed., American Institute of Aeronautics and Astronautics, 2012, Chap. 1, pp. 1–5,185–188.

[2] Brown, R. G., and Hwang, P. Y., *Introduction to Random Signals and Applied Kalman Filtering: with MATLAB Exercises and Solutions*, 4th ed., Wiley, 2012, Vol. 1, Chaps. 4,7, pp. 143–147, 257–260.

[3] CARLSON, N. A., and BERARDUCCI, M. P., "Federated Kalman Filter Simulation Results," *NAVIGATION*, Vol. 41, No. 3, 1994, pp. 297–322. doi:https://doi.org/10.1002/j.2161-4296.1994.tb01882.x, URL https://onlinelibrary.wiley.com/doi/abs/10.1002/j.2161-4296.1994.tb01882.x.

[4] Blom, H., and Bar-Shalom, Y., "The Interacting Multiple Model Algorithm for Systems with Markovian Switching Coefficients," *IEEE Transactions on Automatic Control*, Vol. 33, No. 8, 1988, pp. 780–783. doi:10.1109/9.1299.

[5] Kalman, R. E., "A New Approach to Linear Filtering and Prediction Problems," *Journal of Basic Engineering*, Vol. 82, No. 1, 1960, pp. 35–45. doi:10.1115/1.3662552, URL https://doi.org/10.1115/1.3662552.

[6] Kalman, R. E., and Bucy, R. S., "New Results in Linear Filtering and Prediction Theory," *Journal of Basic Engineering*, Vol. 83, No. 1, 1961, pp. 95–108. doi:10.1115/1.3658902, URL https://doi.org/10.1115/1.3658902.

[7] Grewal, M. S., and Andrews, A. P., "Applications of Kalman Filtering in Aerospace 1960 to the Present [Historical Perspectives]," *IEEE Control Systems Magazine*, Vol. 30, No. 3, 2010, pp. 69–78. doi:10.1109/MCS.2010.936465.

[8] Schmidt, S. F., "The Kalman Filter - Its Recognition and Development for Aerospace Applications," *Journal of Guidance and Control*, Vol. 4, No. 1, 1981, pp. 4–7. doi:10.2514/3.19713, URL https://doi.org/10.2514/3.19713.

[9] Grewal, M. S., and Andrews, A. P., *Kalman Filtering: Theory and Practice Using MATLAB*, 3rd ed., John Wiley and Sons, Inc., Hoboken, New Jersey, 2008, Chap. 1, pp. 20–26.

[10] Grewal, M., Weill, L., and Andrews, A., *Global Positioning Systems, Inertial Navigation, and Integration*, 2nd ed., Wiley, 2007. doi:10.1002/9780470099728.ch3.

[11] Harvey, A. C., and Todd, P. H. J., "Forecasting Economic Time Series with Structural and Box-Jenkins Models: A Case Study," *Journal of Business & Economic Statistics*, Vol. 1, No. 4, 1983, pp. 299–307. doi:10.1080/07350015.1983.10509355, URL https://www.tandfonline.com/doi/abs/10.1080/07350015.1983.10509355.

[12] Harvey, A. C., and Pierse, R. G., "Estimating Missing Observations in Economic Time Series," *Journal of the American Statistical Association*, Vol. 79, No. 385, 1984, pp. 125–131. URL http://www.jstor.org/stable/2288346.

[13] Kitagawa, G., and Gersch, W., "A Smoothness Priors-State Space Modeling of Time Series with Trend and Seasonality," *Journal of the American Statistical Association*, Vol. 79, No. 386, 1984, pp. 378–389. URL http://www.jstor.org/stable/2288279.

[14] Shumway, R. H., and Stoffer, D. S., "An Approach to Time Series Smoothing and Forecasting Using The EM Algorithm," *Journal of Time Series Analysis*, Vol. 3, No. 4, 1982, pp. 253–264. doi:https://doi.org/10.1111/j.1467-9892.1982.tb00349.x, URL https://onlinelibrary.wiley.com/doi/abs/10.1111/j.1467-9892.1982.tb00349.x.

[15] Zihajehzadeh, S., and Park, E. J., "A Novel Biomechanical Model-Aided IMU/UWB Fusion for Magnetometer-Free Lower Body Motion Capture," *IEEE Transactions on Systems, Man, and Cybernetics: Systems*, Vol. 47, No. 6, 2017, pp. 927–938. doi:10.1109/TSMC.2016.2521823.

[16] Balslev, J., and Klok, A. K., "Methods and Systems of a Motion-Capture Body Suit with Wearable Body-Position Sensors," , No. US20170192496A1, 2017.

[17] Li Meng, Liu Li, and Veres, S. M., "Aerodynamic Parameter Estimation of an Unmanned Aerial Vehicle Based on Extended Kalman Filter and Its Higher Order Approach," *2010 2nd International Conference on Advanced Computer Control*, Vol. 5, 2010, pp. 526–531.

[18] Curvo, M., "Estimation of Aircraft Aerodynamic Derivatives Using Extended Kalman Filter," *Journal of the Brazilian Society of Mechanical Sciences*, Vol. 22, 2000, pp. 133 – 148. URL http://www.scielo.br/scielo.php?script=sci_arttext&pid=S0100-73862000000200001&nrm=iso.

[19] Jeffrey Bauer, and Dominick Andrisani, "Estimating Short-Period Dynamics Using an Extended Kalman Filter," *Orbital Debris Conference: Technical Issues andFuture Directions*, 1990. doi:10.2514/6.1990-1277, URL https://arc.aiaa.org/doi/abs/10.2514/6.1990-1277.

[20] Kokolios, A., "Use of a Kalman Filter for the Determination of Aircraft Aerodynamic Characteristics from Flight Test Data," *32nd Aerospace Sciences Meeting and Exhibit*, 1994. doi:10.2514/6.1994-10, URL https://arc.aiaa.org/doi/abs/10.2514/6.1994-10.

[21] Rufus, I., *Differential Games: A Mathematical Theory with Applications to Warfare and Pursuit, Control and Optimization*, the dover ed., General Publishing Company, London, United Kingdom, 1999, Chap. 8, pp. 202–205.

[22] Cockayne, E., "Plane Pursuit with Curvature Constraints," *SIAM Journal on Applied Mathematics*, Vol. 15, No. 6, 1967, pp. 1511–1516. doi:10.1137/0115133, URL https://doi.org/10.1137/0115133.

[23] Rublein, G. T., "On Pursuit with Curvature Constraints," *SIAM Journal on Control*, Vol. 10, No. 1, 1972, pp. 37–39. doi:10.1137/0310003, URL https://doi.org/10.1137/0310003.

[24] Dowdle, J. R., Athans, M., Gully, S. W., and Willsky, A. S., "An Optimal Control and Estimation Algorithm for Missile Endgame Guidance," *1982 21st IEEE Conference on Decision and Control*, 1982, pp. 1128–1132. doi:10.1109/CDC.1982.268329.

[25] Uhrmeister, B., "Kalman Filters for a Missile with Radar and/or Imaging Sensor," *Journal of Guidance, Control, and Dynamics*, Vol. 17, No. 6, 1994, pp. 1339–1344. doi:10.2514/3.21353, URL https://doi.org/10.2514/3.21353.

[26] Angelova, D., and Mihaylova, L., "Joint Target Tracking and Classification with Particle Filtering and Mixture Kalman Filtering Using Kinematic Radar Information," *Digital Signal*

Processing, Vol. 16, No. 2, 2006, pp. 180–204. doi:https://doi.org/10.1016/j.dsp.2005.04.007, URL https://www.sciencedirect.com/science/article/pii/S1051200405000679.

[27] Taur, D.-R., and Chern, J.-S., "A Modified Proportional Navigation Guidance Law for IR Homing Missiles," *AIAA Guidance, Navigation, and Control Conference and Exhibit*, 2000. doi:10.2514/6.2000-4160, URL https://arc.aiaa.org/doi/abs/10.2514/6.2000-4160.

[28] Srinivasan, T., Kar, P. K., Sarkar, A. K., and Ananthasayanam, M. R., "Performance Study of Radar And Seeker Estimator in a Realistic Tactical Scenario," *AIAA Guidance, Navigation and Control Conference and Exhibit*, 2008. doi:10.2514/6.2008-7462, URL https://arc.aiaa.org/doi/abs/10.2514/6.2008-7462.

[29] Sarkar, A., Ananthasayanam, M., Srinivasan, T., and Kar, P., "Comparison of the Radar and Seeker Modes of Pursuer Guidance," *Journal of Guidance Control and Dynamics - J GUID CONTROL DYNAM*, Vol. 32, 2009, pp. 1912–1920. doi:10.2514/1.40404.

[30] Chung, C., and Furukawa, T., "Coordinated Search-and-Capture Using Particle Filters," *Control, Automation, Robotics and Vision*, 2007, pp. 1 – 6. doi:10.1109/ICARCV.2006.345338.

[31] Venkataraman, R., and Seiler, P. J., "Model-Based Detection and Isolation of Rudder Faults for a Small UAS," *AIAA Guidance, Navigation, and Control Conference*, 2015, p. 0857.

[32] Keipour, A., Mousaei, M., and Scherer, S., "Automatic Real-Time Anomaly Detection for Autonomous Aerial Vehicles," *2019 International Conference on Robotics and Automation (ICRA)*, 2019, pp. 5679–5685. doi:10.1109/ICRA.2019.8794286.

[33] Boskovic, J. D., Sai-Ming Li, and Mehra, R. K., "Robust Supervisory Fault-Tolerant Flight Control System," *Proceedings of the 2001 American Control Conference. (Cat. No.01CH37148)*, Vol. 3, 2001, pp. 1815–1820 vol.3.

[34] Hibbeler, R. C., *Engineering Mechanics: Dynamics*, 14th ed., Pearson Prentice Hall, Hoboken, New Jersey, 2015, Chap. 12, pp. 56–58.

[35] Nahin, P., *Chases and Escapes: The Mathematics of Pursuit and Evasion*, Paradoxes, perplexities, and mathematical conundrums for the serious head scratcher, Princeton University Press, 2012. URL https://books.google.com/books?id=vDyUNDjhhwMC.

[36] Cook, B., Arnett, T. J., Macmann, O., and Kumar, M., "Real-Time Radar-Based Tracking and State Estimation of Multiple Non-Conformant Aircraft," *AIAA Information Systems-AIAA Infotech @ Aerospace*, 2017. doi:10.2514/6.2017-1133, URL https://arc.aiaa.org/doi/abs/10.2514/6.2017-1133.

[37] Danz, A., "BoxplotGroup," *MATLAB Central File Exchange*, 2021. URL https://www.mathworks.com/matlabcentral/fileexchange/74437-boxplotgroup.

[38] Klappa, P. J., and Fields, T., "Assessment of Fixed-Wing UAV System Identification Models During Actuator and Payload Drop Failures," *AIAA SciTech 2021 Forum*, 2021. doi:10.2514/6.2021-1529, URL https://arc.aiaa.org/doi/abs/10.2514/6.2021-1529.

[39] Ackerman, E., "Zipline Wants to Bring Medical Drone Delivery to U.S. to Fight COVID-19," *IEEE Spectrum*, 2020. URL https://spectrum.ieee.org/automaton/robotics/drones/zipline-medical-drone-delivery-covid19.

[40] Porter, J., "Zipline's Drones are Delivering Medical Supplies and PPE in North Carolina," *The Verge*, 2020. URL https://www.theverge.com/2020/5/27/21270351/zipline-drones-novant-health-medical-center-hospital-supplies-ppe.

[41] Ojeda, H., "Federal Aviation Administration Investigating University of Iowa Drone Crash," *Iowa City Press-Citizen*, 2020. URL https://www.press-citizen.com/story/news/2020/01/23/faa-investigating-university-iowa-drone-crash/4554292002/.

[42] Meier, L., Honegger, D., and Pollefeys, M., "PX4: A node-based Multithreaded Open Source Robotics Framework for Deeply Embedded Platforms," *2015 IEEE International Conference on Robotics and Automation (ICRA)*, 2015, pp. 6235–6240. doi:10.1109/ICRA.2015.7140074.

[43] Abdulrahim, M., Mohamed, A., and Watkins, S., "Control Strategies for Flight in Extreme Turbulence," *AIAA Guidance, Navigation, and Control Conference*, 2017. doi:10.2514/6.2017-1909.

[44] Nelson, R. C., *Flight Stability and Automatic Control*, 2nd ed., McGraw-Hill, 1998, Chap. 5, pp. 193–195.

[45] Lavretsky, E., and Wise, K., *Robust and Adaptive Control: with Aerospace Applications*, Springer, London, 2013, Chap. 1, pp. 12–16.

[46] Morelli, E. A., and Klein, V., *Aircraft System Identification: Theory and Practice*, 2nd ed., Sunflyte Enterprises, Williamsburg, Virginia, 2016, Chaps. 1,6,11, pp. 1–5,192–193,363–367.

[47] Morelli, E. A., "Flight Test Maneuvers for Efficient Aerodynamic Modeling," *Journal of Aircraft*, Vol. 49, No. 6, 2012, pp. 1857–1867. doi:10.2514/1.C031699, URL https://doi.org/10.2514/1.C031699.

[48] Dorobantu, A., Ozdemir, A. A., Turkoglu, K., Freeman, P., Murch, A., Mettler, B., and Balas, G., "Frequency Domain System Identification for a Small, Low-Cost, Fixed-Wing UAV," *AIAA Guidance, Navigation, and Control Conference*, 2011. doi:10.2514/6.2011-6719, URL https://arc.aiaa.org/doi/abs/10.2514/6.2011-6719.

[49] Grauer, J. A., "Position Corrections for Airspeed and Flow Angle Measurements on Fixed-Wing Aircraft," Tech. rep., NASA, 2017.

[50] Poksawat, P., Wang, L., and Mohamed, A., "Gain Scheduled Attitude Control of Fixed-Wing UAV with Automatic Controller Tuning," *IEEE Transactions on Control Systems Technology*, Vol. 26, No. 4, 2018, pp. 1192–1203. doi:10.1109/TCST.2017.2709274.

VITA

Paul James Klappa was born on June 16, 1997 in St. Louis Park, MN. He attended St. John's elementary school in Hopkins, MN and then attended Hopkins High School in Minnetonka, MN and graduated in 2015. In 2019, he graduated Magna Cum Laude from Rockhurst University with a Bachelor's of Science Degree in Mechanical Engineering. Since graduation, he has worked as a graduate research assistant under Dr. Travis Fields in the Parachute and Aerial Vehicle Systems laboratory. He also worked as a Teacher's Assistant for the Unmanned Robotics Systems course at UMKC and as an Adjunct Faculty Member for Dynamics at Rockhurst University. Paul's research has focused on the implementation of state estimation using onboard and off-board aircraft sensors during nominal and failure flight conditions. After graduation Paul plans to work in the Defense and Aerospace industry.